A spectrometer for depth selective conversion electron Mössbauer spectroscopy

Christopher B. Doner, Department of Physics, McGill University, Montreal

A Thesis submitted to the Faculty of Graduate Studies and Research in partial fulfilment of the requirements of the degree of Masters of Science

Abbreviated title:

A depth selective conversion electron Mossbauer spectrometer

Abstract

A spectrometer was built for the purpose of performing Depth Selective Conversion Electron Mossbauer Spectroscopy [DSCEMS] on surfaces containing iron nuclei. The spectrometer was based on a Retarding Field Analyzer design by van Noort and van Gorkum[1]. It has an acceptance angle of 5% of 4π, and is capable of energy resolutions of between .8% and 4.3% of the pass energy. The spectrometer is suited for samples with a diameter as large as 10 mm. The designing and dimensioning processes, construction, operation, and performance of the spectrometer are presented here.

Resumé

Un spectromètre a été bâti dans le but d'effectuer la spectroscopie de Mossbauer d'électron de conversion avec sélection de profondeur sur des surfaces contenant des noyanx de fer. Le spectomètre est basé sur l'analyseur à champs retardé de van Noort et van Gorkum[1]. Il a un angle d'acceptance de 5% de 4π, et une résolution en énergie di 0,8 à 4.3% de l'énergie de passe. Le spectromètre peut accepter des échantillons de diamètres allant jusqu'à 10 mm. Nous allons décrive ici les processus du design et de la construction, l'opération, et la performance du spectromètre.

Acknowledgements

I would like to acknowledge the important contributions of Dr. Richard Fernholz who designed all of the critical components of the system (vacuum chamber and the grid assembly). His first class technical drawings, and practical knowledge were the foundation of the project.

I gratefully acknowledge the efforts of John Egyed, Michael Champagne, and all of the technical staff in the workshop. The vacuum chamber, table, and all of the spectrometer parts were constructed in the workshop. Their knowledge, speed, and expertise greatly aided the project.

I thank Frank van Gils for communicating with the Dutch group that built the spectrometer on which our design was based. Frank's uncanny ability to know where to find things was also greatly appreciated.

I thank Xian Bian who carefully guided me through the sputtering processes, and Joe McDermid in engineering who carefully guided me through the annealing process for the cones.

Mostly, I would like to thank my supervisor, Professor Dominic Ryan, whose guidance and effort saw the project through. His knowledge, sharp thinking, and assertiveness, were an inspiration.

Dedication

This thesis is dedicated to my foster brothers, who taught me that a little bit of chaos is a good thing.

DANNY BARRETT
JOHN COTTON
JIMMY COX
WESLEY CRIDDLE
KIM DARNBY
MARTIN DILLION
CHUCK FANNON
CHERYL HARE
KEN HUNT
ANDY LEBREQUE
BROCK MCKENZIE
JOHN MISCAMPBELL
LEWIS MORRISON
SCOTT PATTERSON
JERRY PERSICO
TIM POTTER
SCOTT SANDERSON
MIKE SPIERS
LEVON THALIN
RICK VENT
DOUG WAUGH
MARK WEST

TABLE OF CONTENTS

LIST OF FIGURES

LIST OF TABLES

Chapter 1: Introduction

1.1 Overview for the Project

The aim of the project was to build an electron spectrometer with characteristics such that Mossbauer spectra, derived from conversion electrons emitted at different depths from the sample's surface, could be obtained. These spectra would provide information on the hyperfine structure of Mossbauer nuclei at specific depth ranges within ~100 nm of the sample's surface. For instance, a spectra could be obtained pertaining to the environment within the first ~20 nm from the sample's surface, and a second could be obtained pertaining to the next ~20 nm, and so on. The spectra obtained would provide, in effect, a depth profile of the first ~100 nm of the sample's thickness.

Depth profiling has many potentially important applications for samples containing Mossbauer nuclei. It would enable the experimenter to identify, and examine multi-layer surfaces. For instance, in corrosion processes oxide surfaces could be analyzed, and this could reap benefits to the steel industry. Mossbauer spectra relate information about direction and magnitude of magnetic fields, and the occupation of crystallographic positions, and obtaining this information as a function of depth has resulted in important contributions to surface science. Moreover, the information is obtained in a non-destructive manner unlike many conventional testing methods.

The presentation of this thesis proceeds as follows. The first chapter reviews conventional transmission Mossbauer spectroscopy, and leads into a discussion of the requirements of a spectrometer for Depth Selective Conversion Electron Mossbauer Spectroscopy [DSCEMS]. It gives a review of previously employed DSCEMS spectrometer designs, including a detailed review of the spectrometer by van Noort and van Gorkum which served as the basis for our design. The second chapter begins with an explanation of the reasons for choosing the design, and identifies the changes that were made from the original design. The remainder of the chapter is devoted to describing, and then giving results from, the computer programs written to characterize spectrometer performance, and determine the effects of dimensional changes.

The third chapter provides a detailed description of the assembly of the apparatus, and in particular gives an account of the techniques used to fabricate the grids. The fourth chapter explains the operating controls for the voltages applied to the grids and detector. It gives an account of the safety features that were built into the apparatus, and presents the vacuum and detector characteristics. It also gives an account of the sample changing procedure.

The fifth chapter characterizes the sources of background, and the samples that were to be tested. It also presents the observed spectra from the chosen samples. The sixth chapter compares the spectrometer's experimental performance to that predicted by the computer, and analyses the signal count rates obtained. The seventh chapter consists of suggestions to bring about improvements to the performance.

The contributions of the author to the project is as follows:

- wrote computer programs to find the effects of dimensional changes to spectrometer performance, and thereby established acceptable dimensions
- etched grid in focusing lens
- assembled the system, including wiring, wrapping the cylindrical mesh, and gluing the other grids
- designed detector, and sample mounts, and supervised their construction in the workshop
- built controls for vacuum system, voltage system, and safety systems
- wrote operator's manual for system
- performed all of the experimental tests of the system

1.2 Conventional Transmission Mossbauer Spectroscopy for the Study of Hyperfine Structure

Photons incident upon a target atom can only be resonantly absorbed if their energy is equal to that of an atomic or nuclear transition within the target atom. There is a fundamental difference between resonant absorption in nuclear transitions and in atomic transitions. That is, because excited nuclear states are much further from their ground state than are excited optical states, the recoil energy becomes significant, as will be shown. It is the Mossbauer effect which, for atoms bound within a solid, effectively eliminates the recoil energy, making resonant absorption a practical experimental possibility, and in so doing, provides an opportunity for much experimental study of solids.

This will become apparent in the following text.

If a free atom is considered, an emitted photon must be of slightly less energy than the splitting between energy states due to the recoil energy imparted on the atom. If an emitted quantum is considered where E_1 is the energy above the ground state of the excited state, and E_γ is the energy of the photon, then by conservation of momentum, the recoil momentum of the atom must equal the momentum of the photon, E_γ/c. The recoil energy of the atom is then,

$$E_R = \frac{p_R^2}{2M} = \frac{E_\gamma^2}{2Mc^2} \approx \frac{E_1^2}{2Mc^2} \qquad (1.1)$$

In the case of absorption, the recoil momentum is in the same direction as the photon involved, and hence, the incident photon must again supply the recoil energy. So that in addition to E_1, the incident photon must supply twice the recoil energy in order to obtain resonant absorption. The incident photon must therefore have energy, $E_\gamma \approx E_1 + E_1^2/Mc^2$.

If we now compare the natural linewidth, to the recoil energy in the atomic and the nuclear cases of ^{57}Fe, it becomes apparent that the recoil energy is insignificant in the atomic case, but not in the nuclear case. In both cases, the lifetime of the excited states is $\sim 10^{-7}$ seconds, and according to the uncertainty principle, this corresponds to a natural linewidth of $\sim 10^{-8}$ eV. (For the purposes of numerical comparison, and because of its relevance to the project at hand, the ^{57}Fe example will be employed exclusively in the following discussion. There is though, a long list of isotopes for which the Mossbauer effect has been observed.) For atomic transitions, E_1 ranges from 1.8 eV to 8 eV so that for M=57 a.m.u., the recoil energy can range from $3x10^{-11}$ to $6x10^{-10}$ eV. That is, the linewidth is too large for the recoil energy to have significance. On the other hand, the most used nuclear transition, corresponds to E_1=$1.44x10^4$ eV (see Figure 1.1), and hence the recoil energy is $1.9x10^{-3}$eV. That is, the recoil energy is much larger than the natural linewidth.

For atoms bound within a solid though, the Mossbauer effect occurs, which results in recoilless resonant absorption. The effect is due to the fact that in a solid, the recoil must result in lattice vibrations, phonons. If we consider an Einstein solid with 3N independent vibrational modes, all of frequency ω, then the minimum excitation energy, $\hbar\omega$, for a mode is $\sim k\theta_D=4.2x10^{-2}$ eV. By comparison, the free atom recoil energy is $1.9x10^{-3}$ eV. A large probability thus exists that a phonon will not be excited, and the entire solid will have to recoil as a unit. In this case, the mass, M, in the expression for the recoil energy becomes the mass of the sample, and hence, the recoil energy becomes negligible.

The fraction of nuclei which absorb a photon without resulting in a lattice vibration is called the recoil free fraction, f. The following expression is an accurate representation of f in a strong lattice[2].

$$f = \exp\left(-\frac{3}{2}\frac{E_R}{k\theta_D}\left[1 + 4\left(\frac{T}{\theta_D}\right)^2\int_0^{\frac{\theta_D}{T}}\frac{x\,dx}{e^x-1}\right]\right) \qquad (1.2)$$

E_R is the recoil energy in Joules, T the temperature in Kelvin, θ_D the characteristic Debye temperature in Kelvin, and k is the Boltzmann constant (1.381×10^{-23} J/K). A complete quantum mechanical derivation of (1.2) can be found in [3].The important physical points to note about (1.2) are that the recoil free fraction can be increased by a)reducing the temperature of the solid, b)choosing nuclei with low energy excited states such that E_1 (and thus E_R), will be minimized and c)choosing hard lattice hosts (i.e. high θ_D).

In order to use the Mossbauer effect to probe the hyperfine structure of the nuclei, several experimental criteria must be met. Firstly, incident gamma rays of energy E_1 are required, and they must be more narrow than the hyperfine splittings. Secondly, a method must be found to add known amounts of energy to the incident rays, so that the hyperfine splittings may be scanned through. Thirdly, a detection system is needed which will determine, in correlation with the added scanning energies, when resonant absorption is taking place.

The first criterion, that of supplying gamma rays of energy E_1, is achieved through the use of unstable nuclei which decay into the studied nuclei, through a metastable state which is the same as the excited state of the studied nuclei. In about 91% of all cases, ^{57}Co decays into unstable ^{57}Fe through a 14.4 keV state to the ground state of ^{57}Fe, as can be seen in Figure 1.1. The unstable nuclei must be incorporated into a suitable host. That is, one that will leave the nuclear levels unsplit. Any cubic, diamagnetic or paramagnetic metal, into which the ^{57}Co may enter in a substitutional manner will fulfil this requirement. Rhodium, and palladium are the two most frequently employed hosts. The combination of the unstable nuclei in the host is referred to as the source.

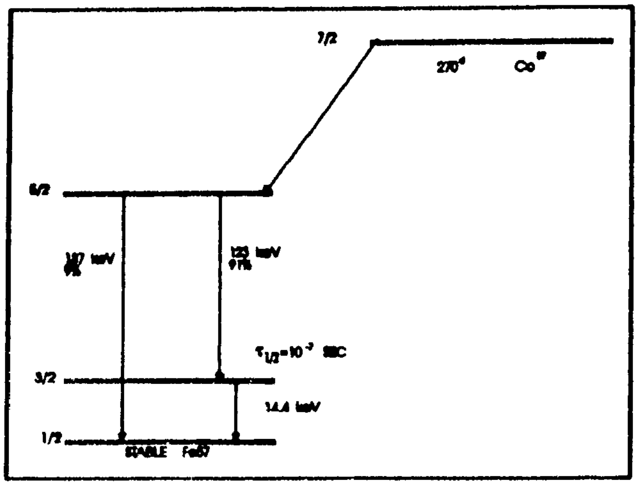

Figure 1.1 Decay of ^{57}Co to ^{57}Fe

The second criterion, that of adding (or subtracting) known amounts of energy to the incident gamma rays, is accomplished by Doppler shifting the gamma rays. The shifting is accomplished by mounting the source in a velocity transducer. A velocity of ±10 mm/s is enough to scan the hyperfine structure of the ^{57}Fe nuclei. These modest speeds can be accomplished with the use of a simple mechanical transducer with a programmable feedback system to provide accurate velocity control.

The third criterion, that of an adequate detection system, is accomplished through the use of the fact that a significant portion of the incident gamma rays that would ordinarily pass through the sample will not pass when resonance is achieved due to their absorption within the sample. To measure the transmission, a simple proportional counter detector is used. There is a wire anode within the detector at a potential of ~1700 volts which represents ~140 times the ionization potential of the counting gas.

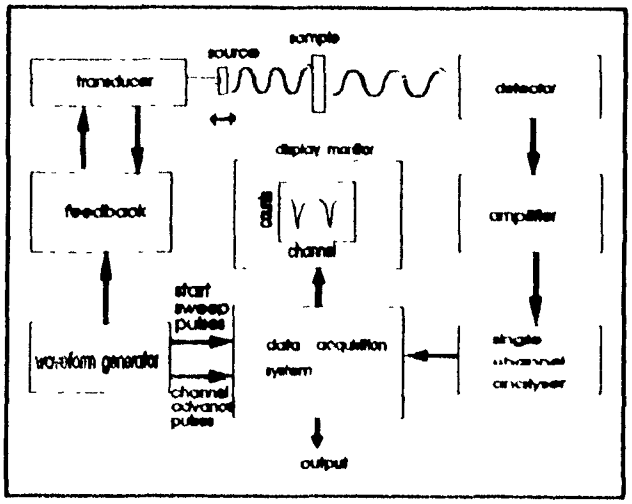

Figure 1.2 Set-up for Transmission Mossbauer Spectroscopy

When an incident γ-photon ionizes a counting gas molecule, freed electrons are accelerated towards the anode. If these electrons are within a critical radius (~1mm) of the anode, a Townsend avalanche will occur in which thousands of electrons are freed in a cascade, and the result is a voltage pulse at the anode (a more complete description of a proportional counter is given in section 1.4). A preamplifier shapes the pulses, and they are sent to an amplifier, and then to a single channel analyzer [SCA]. The SCA passes only those pulses within a height range which corresponds to the 14.4 keV γ-rays. The 122keV and 136keV γ-rays produce larger pulses since a higher energy photon adds more energy to the system causing more ionizations to occur. The pulses that pass through the SCA go to the multichannel scaler [MCS] which sorts and stores the data into a set of channels. The advancement of channels, and sweeps across the set of channels, are determined by pulses that are synchronized with a digital triangular waveform generator. The MCS thereby collects data for equal amounts of time on each channel. The digital waveform also determines the velocity of the source through the use of a feedback loop between the source velocity, and the waveform. Each channel thus corresponds to a particular velocity of the source. The general set-up is shown in

Figure 1.2.

The great usefulness of the Mossbauer effect is due to the fact that the fractional width of the emitted γ-rays is only $3x10^{-13}$ ($13x10^{-9}$eV/14.4keV). Typically, the hyperfine interactions are about 10^{-6} eV, so that a fractional width of $3x10^{-13}$ will allow for an extremely fine study the hyperfine splittings. The extraordinarily small fractional width of the gamma ray make it the most accurately defined electromagnetic radiation available for experimental work.

A brief word should be mentioned about the uses of and the basic variables involved in Mossbauer spectroscopy. There are three basic hyperfine interactions, the isomer shift, the quadrupole splitting, and the magnetic dipole splitting. Each of them provides a tool for studying the local environments of the Mossbauer nuclei. Mossbauer studies employed in conjunction with x-ray diffraction and other structural studies, have resulted in the accumulation of a vast and important body of information concerning lattice structures, bonding arrangements within solids, and electric and magnetic fields within matter. The overall trends observed, have contributed to our general understanding of electron behaviour within solids.

The isomer shift is due to the electric monopole interaction between the nuclear charge distribution and the electronic charge distribution over the finite volume of the nucleus. The isomer shift allows the experimenter to observe how the electron density changes at the Mossbauer nucleus in different lattices, and in

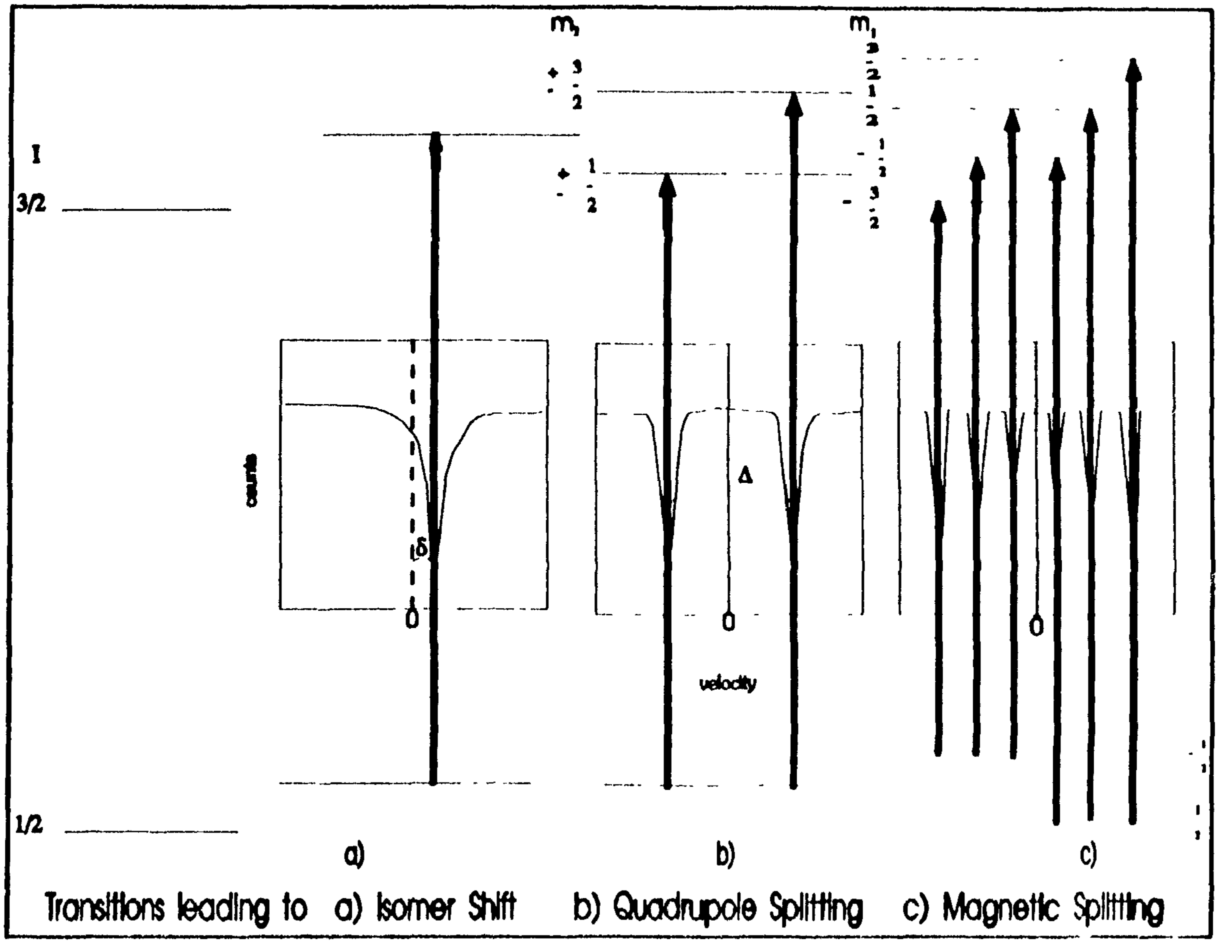

Figure 1.3 Hyperfine Interactions

different lattice sites. The isomer shift is not an absolute quantity. δ as shown in Figure 1.3a) represents the difference in the electric monopole interaction within the source, compared to that within the sample. Usually though, δ refers to the difference in the interaction within the sample, as compared to that within some standardized sample, such as α-Fe. The interaction over the volume of the nucleus can only involve the s orbitals since only the s orbitals have finite probability densities within the nucleus, and hence, these orbitals determine δ. Changes in the isomer shift may be due to interrelated changes in, the number of valence s electrons (in particular there are often large shifts due to s valence electrons being captured by neighbouring atoms), mixing of s electron orbitals through bonding, or shielding effects from p, d, and f electrons on the s electrons.

The quadrupole splitting is due to the interaction between the electric field gradient at the Mossbauer nuclei, and the nuclear quadrupole moment. A nucleus with angular momentum quantum number $I > \frac{1}{2}$ has a non-spherical charge distribution which will interact with an asymmetric electronic charge distribution giving rise to quadrupole splitting. The quadrupole splitting is represented by the symbol, Δ, as shown in Figure 1.3b). Since for a given state, the quadrupole moment is fixed, the splitting gives direct information on the asymmetry of the electronic structure. The asymmetry may be due to several interdependent factors, such as partly filled electronic shells being filled by valence electrons, an asymmetric arrangement of ligand atoms, and/or molecular orbital effects.

The magnetic dipole splitting is due to the interaction between the nuclear magnetic moment and any magnetic field that exists at the nucleus. Figure 1.3c) shows the magnetic splittings for ^{57}Fe. A brief analysis of this spectrum will reveal the most basic parameters involved. For $I > 0$, each state splits into $2I+1$ substates. A transition rule states that transition changes wherein m_I differs by more than one are not possible, and hence, there is a limit of six possible transitions. The peak intensities are in the ratios 3:2:1:1:2:3. These ratios are representative of an isotropic distribution of magnetic field directions at the nuclei, and in general, the ratios are determined by the orientation of the magnetic field at the Mossbauer nuclei. The amount of splitting for a particular nuclear magnetic dipole moment is determined by the strength of the field at the nuclei. There are thus two pieces of information that can be obtained from the magnetic splittings 1)the intensity ratios determine the orientation of the field, 2)the amount of splitting determines the strength of the field. In addition, but of lesser practical importance, the number of lines gives information as to what states are involved (each state splits into 2I+1 substates).

1.3 Conversion Electron Mossbauer Spectroscopy (CEMS)

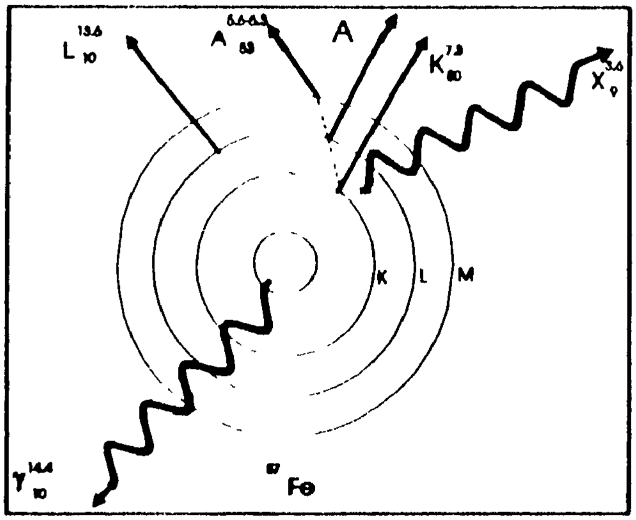

Figure 1.4 The Internal Conversion Process of ^{57}Fe

In only about 10% of the events involving the absorption of the 14.4 keV photons does the nucleus re-emit a gamma quantum of the same energy as the one that excited it. In the other 90% of the events, a process known as internal conversion occurs (see Figure 1.4). In this process a K-shell electron is emitted. The K-shell electron will have a kinetic energy equal to the excitation energy less its binding energy. That is, the electron will have a fixed kinetic energy of 7.3 keV. Since the emission of this electron will leave a hole in the K-shell, another electron from the atom will fill its place. This drop will cause a further release of energy, perhaps an X-ray quantum, or an Auger electron. In effect then, there is a cascade until all of the excitation energy has dissipated. Detecting all of the emitted electrons as a function of source velocity will result in a Mossbauer spectrum. The conventional type of CEMS used is integral CEMS or ICEMS, and it involves the detection of all emerging electrons regardless of energy.

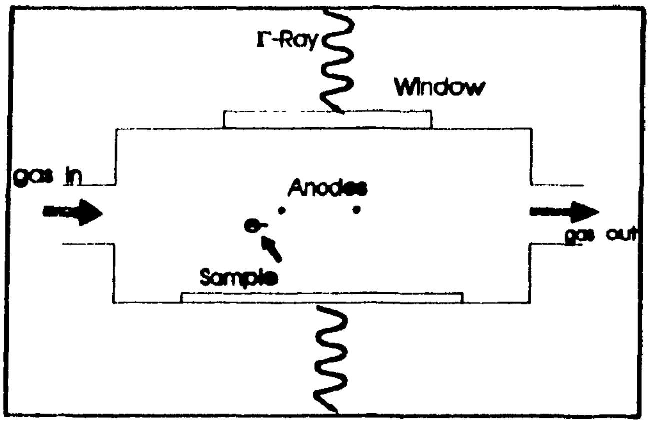

Figure 1.5 A Typical CEMS Detector

Detection of electrons in ICEMS is accomplished with a specialized proportional counter as in Figure 1.5. Gamma rays enter through the window and strike the sample, producing conversion electrons, Auger electrons, X-rays, and γ-rays. The counting gas particles can be ionized either by photons or electrons, but only ionizations within a critical radius (~1 mm) of the wire anodes can produce a pulse, since only in this region is the field strong enough to produce a avalanche. Typically, the counting gas is a mixture of 94% He_2 and 6% CH_4. Helium is used because it has a small cross-section and so the x-rays and γ-rays pass through the detector with minimal ionizations. Methane is the quenching component. The rather large quenching particles tend to absorb the fluorescent emissions of the noble gas particles and have smaller excitation potentials so that their de-excitation photons have insufficient energy to ionize the gas and propagate the discharge further, which could otherwise result in secondary uncorrelated pulses.

There are three important advantages to ICEMS compared to conventional transmission Mossbauer spectroscopy. The first and most important is that CEMS is a surface sensitive technique. That is, the conversion and Auger electrons have a finite range within the absorber material since their energy is dissipated as they travel through the sample. Typically, the electron range is about 300 nm, so the Mossbauer spectrum will correspond to a weighted average of the nuclear environments within this range.

The second advantage of CEMS is that it can be performed with bulk samples. Conventional transmission spectroscopy requires thin absorber specimens (~20 microns thick), or powders. The gamma rays must be able to pass through the sample unobstructed when slightly off resonance, in order to observe resonance, and hence thin samples are required. It is often difficult to prepare such samples without destroying the sample, and therefore, CEMS provides a means for non-destructive testing of thick samples.

The third advantage of ICEMS is that it is statistically effective. The background in transmission spectroscopy increases more dramatically as the proportion of Mossbauer nuclei decreases than in conversion electron spectroscopy. In transmission spectroscopy, the γ-rays that are not absorbed lead directly to background, whereas in conversion electron spectroscopy, most of the background produced is caused by secondary photoelectron processes since the counting gas used (He_2) has a small cross section and is not likely to be directly ionized. Internal conversion occurs in 90% of resonant events producing a cascade of detectable electrons, and hence, there is only about a 10% chance that a resonant event will not produce a signal. Reduction in the signal for conversion electron spectroscopy will therefore be primarily due to the reduced effective thickness (~300 nm) due to the absorbtion of electrons within the sample. In instances where the recoil free fraction is small, Mossbauer spectra can not be obtained with transmission spectroscopy, and ICEMS must be employed.

There are though, several good reasons why conventional transmission spectroscopy is more widely employed than CEMS. For one, it requires simpler equipment. The difference being that ICEMS demands that the absorber be located within the proportional counter detector. That is, since electrons are being detected, there is no possibility of having them travel through a solid into the detector, as was the case with gamma rays. Furthermore, low temperature spectra can not be obtained because it is difficult to cool the sample in the gaseous environment. Furthermore, the quenching component of the counting gas condenses on the sample, and since, CEMS is a surface study, the desired spectra can not be obtained. The difficulty in performing ICEMS on samples at less than room temperature limits its wide spread usage.

It should be noted that there is a significant amount of background due to non-resonant photoelectrons, and some due to the incident γ-rays ionizing the counting gas. The mount for the sample should be coated with a layer of aluminum, or another metal with a low secondary electron emission coefficient, so that photoelectrons created by the γ-rays striking the mount are minimized. The background, due to the incident γ-rays ionizing the counting gas directly, can must be minimized by using a thin detector (~5mm), and by using a counting gas with a small cross-section.

1.4 Depth Selective Conversion Electron Mossbauer Spectroscopy (DSCEMS)

Using an electron spectrometer, it is possible to count only those conversion electrons lying within a particular energy window. In particular, approximately 10% of all conversion electrons are initially emitted with an energy of 7.3 keV, and these electrons will lose energy through collisions as they travel towards the surface of the sample. By counting electrons that are emitted with pass energies near 7.3 keV, it is possible to obtain Mossbauer spectra corresponding to the nuclear environments at narrow depth ranges extremely close to the sample surface. The physical requirements of such a spectrometer are however, considerably more demanding than the requirements of a ICEMS apparatus.

The basic components that a DSCEMS spectrometer must consist of are: a sample, an energy selecting device, and a detector. Furthermore, these all must be under vacuum, since the energy selection required is too fine for the use of a counting gas. The vacuum also facilitates the ability to perform temperature dependent studies. Radiation must enter the vacuum and strike the sample, causing the emission of electrons. A device, which can focus the electrons with some combination of magnetic and/or electric fields, must then select electrons in the desired energy range, onto a detector. The detector must be some sort of electron-multiplying mechanism, which will send pulses out of the vacuum to a data acquisition system.

The fundamental physical difficulty which must be overcome in designing a spectrometer for DSCEMS is the shortage of electrons to count. Whereas in ICEMS systems, electrons may be detected over a solid angle of 2π and may be emitted up to about 300 nm beneath the surface of the sample, in the DSCEMS systems designed to date, electrons are detected over a solid angle of at most 13% of 2π and depths of at most 100 nm below the surface of the sample, and hence, there is an immediate reduction of at least a factor of 23 in the available intensity. Furthermore, DSCEMS does not receive signal from lower energy electrons including lower energy conversion electrons, Auger electrons, and those electrons generated as a result of the numerous collisions of the conversion electrons as they travel through the sample. For samples of the same surface area and content, the rate of electron detection will be at least 100 times less in DSCEMS than in ICEMS.

By minimizing the number of loses of available electrons, a high performance DSCEMS spectrometer will attain maximum luminosity. The luminosity may be defined as the product of, the sample surface area, and the transmission. The transmission is defined here as the ratio of the emergent flux of electrons of a specific energy, to the flux which enters the spectrometer. It includes the solid angle acceptance area as a fraction of 4π, and any blocking fractions due to grids or apertures that are in the path of the elections. The luminosity has dimensions of area, and represents a reasonable criterion for comparing the overall effectiveness of spectrometers. In some cases though, owing partly to effects which stem from variations in the angular region at which the spectrometer detects electrons, and partly due to detector efficiency, it is necessary to make a more detailed comparison.

The basic constraint involved in designing a DSCEMS spectrometer is that electron count rate is purchased at the expense of energy resolution. That is, one can detect more electrons if there is a larger base of detectable electrons. Typical DSCEMS spectrometers have energy resolutions between 1% and 10%. Liljequist and Ekdahl[4] have shown that an energy resolution less than 1% does not improve the depth selectivity. For resolutions above 1% though, smaller resolutions will result in better depth profiling and of course, longer counting times. A spectrometer which features resolution control in the 1% to 15% range, will have the greatest applicability. Resolutions above 15% are not suited to DSCEMS, since lower energy (6.3 keV) Auger electrons will be detected which originate from nearer to the surface than the desired K conversion electrons, and will thus destroy the depth profiling.

Naturally, a spectrometer which does not distort the Mossbauer spectrum will be more desirable. The two most common distortions are 1) magnetic hyperfine splittings created due to magnetic fields within the spectrometer, and 2) linewidth broadening due to a) unintentional vibrational motions of the sample (usually caused by the pumping system),and b) components of incident γ-ray trajectories which are not parallel to the Doppler shifting velocities imparted to the source. The first distortion can be eliminated by employing electrostatic fields rather than magnetic fields to provide energy selection. Magnetic spectrometers have been employed by several groups to demonstrate DSCEMS, but the magnetic hyperfine splittings created pose inconveniences for more detailed studies. Many spectrometers also use Helmholz coils to cancel the earth's magnetic field. Linewidth broadening due to vibrations of the sample can be effectively eliminated by first decoupling external vibrations from the source and sample, and then ensuring that the source and sample are joined in a rigid manner. Broadening due to γ-rays which are non-parallel to the transducer velocity is dependent upon the diameters of the source and sample, and the source-sample distance. In the case of the our spectrometer, a 6 mm diameter source, located 75 mm from a 10 mm diameter sample, can produce broadening of not more than 1%.

In the case where ^{57}Fe is the Mossbauer nucleus, the spectrometer must be able to detect electrons with energies varying from above the maximum Auger electron energy (>6.3 keV) to the maximum K conversion electron energy (7.3 keV). Liljequist refers to this as the APK (Almost Pure K-conversion) interval[5]. A superior spectrometer would though, be able to analyze other isotopes. Sn would be the most popular choice, and it would require the detection of electrons with energies up to 19.6 keV.

Other desirable features of a DSCEMS spectrometer are, the ability to measure high and low temperature spectra, the facility to change samples without breaking vacuum, and the ability to isolate particular angular intervals over which electrons emerging from the sample are detected. The latter quality is related to the fact that Liljequist's data[6] demonstrates that spectra derived from the first surface monolayer could be isolated by detecting only electrons that are emitted at glancing angles. Naturally, a simple and economical design is also a very important criterion, though most DSCEMS spectrometers have required difficult construction, at high cost. It is also advantageous to build a spectrometer which operates under ultra-high vacuum so that clean surfaces at low temperatures may be studied.

1.5 The Correspondence Between Depth and the Emitted Electron Distribution

The calculation of electron distributions emitted from a sample is quite complex. A simple but reliable model for electron transport is needed, and then the statistics must be worked out for various crystal structures, and various absorber nuclei. The first theories to provide interpretation of CEMS spectra concentrated on the Mossbauer aspect. That is, Krakowski and Miller[7], Bainbridge[8], and Huffman[9] employed, in slightly different ways, simple exponential relationships to model the electron transport through the sample, neglecting important contributions to the total electron distribution. The most successful analysis, in terms of its agreement with experiment was performed by Liljequist et al. using Monte Carlo simulations[10]. In effect, individual theoretical electron trajectories are traced and statistically analyzed, based on a random generation of electrons within a specific material of averaged properties. The simulations are based on two processes of fundamental importance. One is the stopping power, which is equal to the average energy loss in a collision, and the other is the transport mean free path (it is the inverse of the average scattering per unit path length). These two contributions are representative of the processes in which the electron loses energy and changes direction during a collision. Other processes, which depend upon the variations from the average behaviour, such as classical straggling, are then considered as secondary contributions (most calculations would not include this contribution).

From the view of designing a DSCEMS spectrometer, the results from Liljequist's research which are the most relevant to the design of a DSCEMS spectrometer, concern the angular distribution of the emitted electrons. It was found that it should be possible to selectively observe a surface layer of mean depth <1 nm by only detecting electrons at extreme glancing angles, (θ=80°-90°). The spherical condenser spectrometer (see Figure 1.0) detects electrons in this angular region. In a subsequent paper, the ability to observe very narrow surface layers by detecting glancing angle electrons, was shown to only have usefulness if the surface was such that average surface roughness inclination angle was <5°[11]. On the other hand, the optimum method to obtain spectra from depths >100 Å is to only detect electrons from near perpendicular angles. Basically, electrons from larger depths suffer more scattering, and this variation changes the distribution of emerging electrons from a relatively isotropic one, into one which has an approximately cosθ distribution. A design which detects electrons which are orientated at a near to perpendicular angle from the sample surface will optimize the number of available electrons, but will have lessened depth selectivity. Overall, the spectrometer design needs to be chosen according to the needs of the experimenter, and the samples to be analyzed. If the number of resonant events is small, or narrow depth selectivity is not required, then an acceptance region which is nearly perpendicular to the sample would be preferable in order to maximize the number of detectable electrons. On the other hand, if very thin (<10Å) layers (perhaps oxides or artificially grown films) are to be studied, a glancing angle acceptance region would be preferable.

1.6 Review of DSCEMS Spectrometer Designs

There has been a wide variety of DSCEMS spectrometers built. The first were magnetic devices, converted from existing Gerholm type beta-ray spectrometers[12],[13],[14],[15]. These early devices, aside from their inherent problems associated with the magnetic field present, were not as efficient at combining high luminosity with medium-high energy resolution. They require small sources, have poor transmission characteristics, and can only detect electrons emitted at near to perpendicular orientations which limits their experimental range. The commercial spectrometer of this type employed by the Shigematsu group[15] had a luminosity of .1 mm^2, for a resolution of 2%.

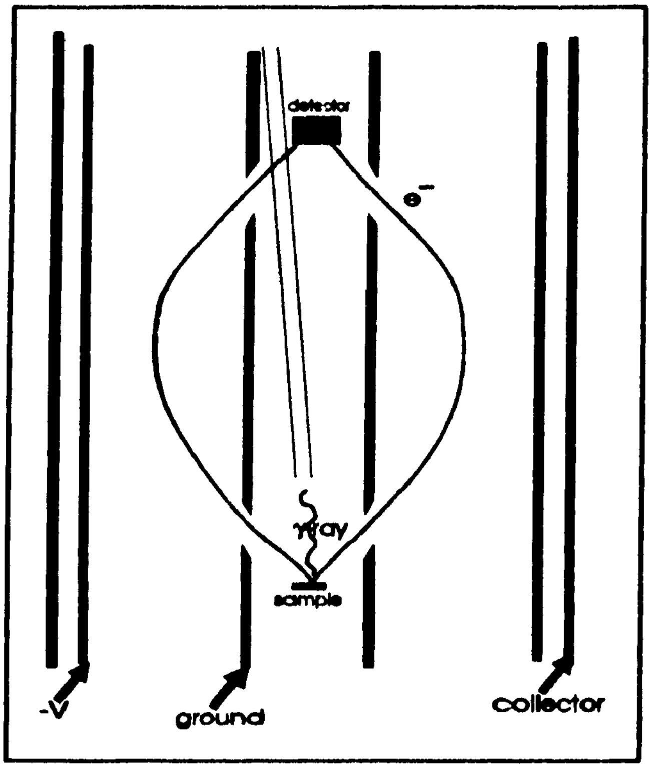

Figure 1.6 A CMA Spectrometer

Several electrostatic Cylindrical Mirror Analyzer (CMA) spectrometers have been used [16,17,18]. Commercial CMA spectrometers are not suited to DSCEMS since they are designed for high resolution applications (~.05%), such as Auger electron spectroscopy, in which there is a much larger quantity of available electrons. Baverstam et al.[19] performed an extensive search to determine the dimensions of a CMA spectrometer that would maximize the performance, and this research was used in the design of subsequent CMAs. The Baverstam group was able to obtain a luminosity of slightly less than 6 mm^2 for a resolution of 2.5%.

Toriyama et al.[20], and Domke et al.[21] constructed retarding reflecting grid spectrometers as shown schematically in Figure 1.7 and Figure 1.8. The device constructed by the Toriyama group was able to obtain a luminosity of .69 mm^2 for a resolution of 2%. Its construction appears to be quite complex. Domke's spectrometer seems to be of simpler construction, but fabrication of spherical surfaces presents several difficulties. The Domke spectrometer was able to obtain a luminosity of about 6.9 mm^2, but was unable to perform at resolutions below 9%.

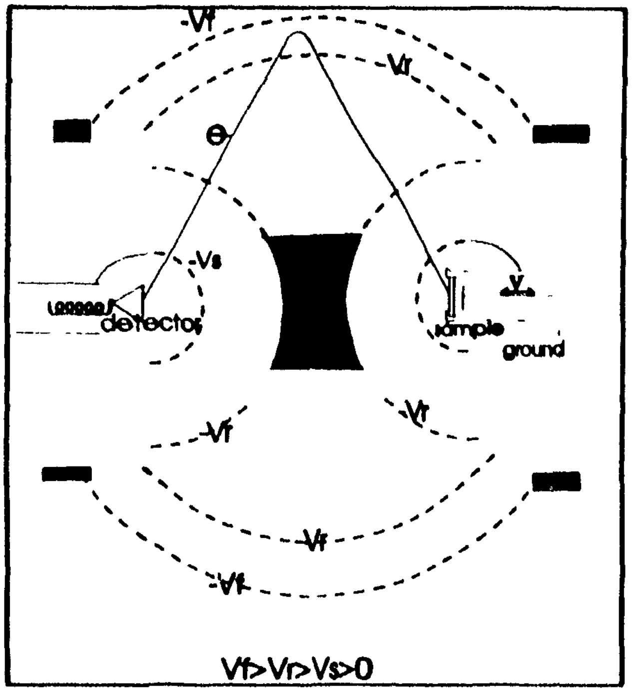

Figure 1.7 Toriyama et al. Retarding Grid Spectrometer

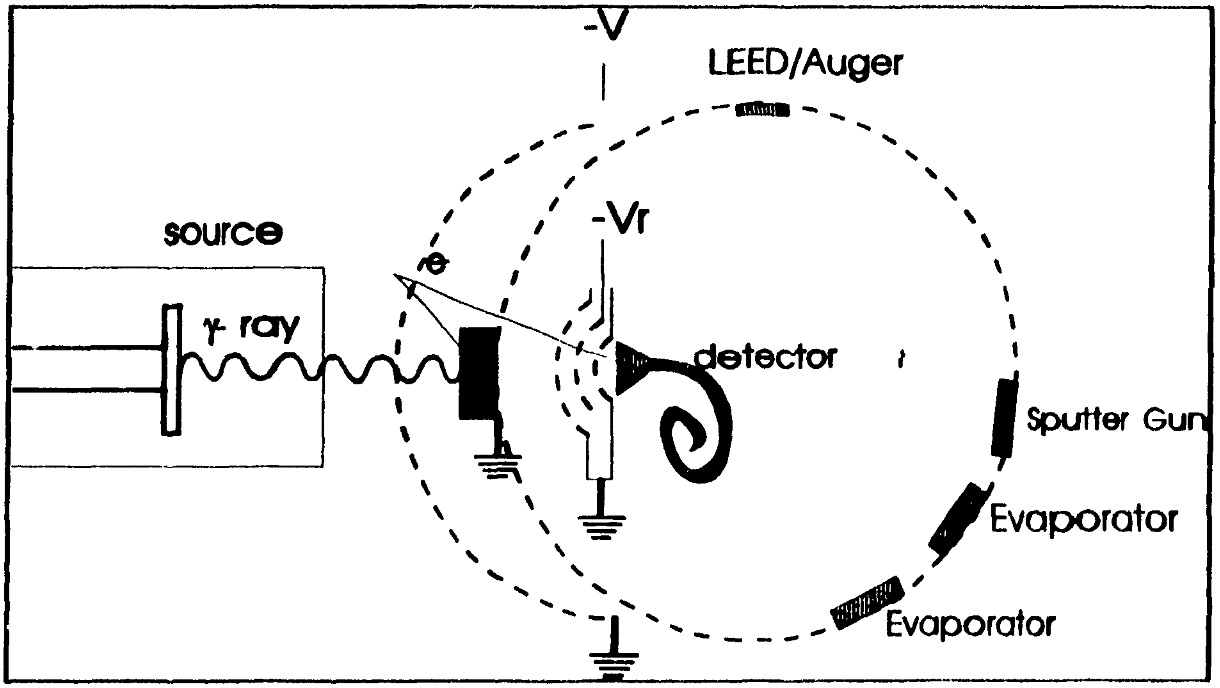

Figure 1.8 Domke et al. Retarding Reflecting Grid Spectrometer

Yang et al.[22] and also Stadnik et al.[43], fabricated spherical condenser spectrometers as shown in Figure 1.9. These spectrometers only detect electrons which are emitted from the sample at glancing angles. This allows for greater depth selectivity, but the density of electrons emitted at glancing angles is less than that at perpendicular angles. They have the largest luminosity of any spectrometers made to date. For an energy resolution of 2.1%, both spectrometers have a luminosity of 11.4mm^2. However, if we assume an average angle of emission of 80°, and adjust for the cosθ distribution, the effective luminosity is only 2mm^2. The difficult construction of spherical surfaces is one of the drawbacks of the design. It is also not compatible with other surface analytic techniques such as Auger and XPS. Furthermore, its absorber is located within the field of the spectrometer, and according to van Noort et al.[24], it is difficult to bombard the sample with γ-rays in this arrangement without disturbing the electric field.

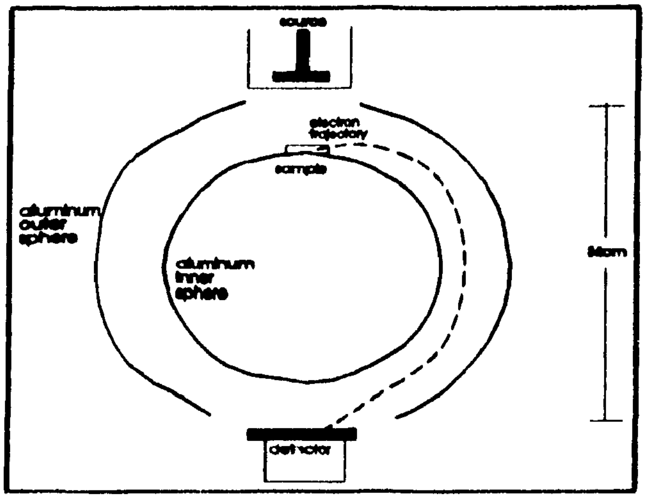

Figure 1.9 Yang et al. Spherical Electrostatic Spectrometer

Table 1.1 Comparison of Spectrometer Performance Characteristics

Group and Spectrometer Type	Resolution (%)	Transmission (% of 4π)	Sample Size (diameter in mm)	Range of Accepted Angles[1] (°)	Luminosity (mm^2)
Shigematsu, commercial 150° spherical sector	2	.27	7	10-20	.1
Baverstam, CMA	2.5	6	5	38-48	5.6
Toriyama, Spherical Retarding Grid	2 1 .3	5.5 2.1 1.2	4 4 3	30-90 30-60 30-60	.69 .26 .085
Domke, Spherical Retarding Reflecting Grid	9	35	5	10-90	6.9
Yang, Spherical Electrostatic	2	13	10	75-90	11.4
Stadnik, Spherical Electrostatic	2.1	13	10	75-90	11.4
van Noort, RFA	2	5	10	0-80	3.9

[1] This does not refer to a point source acceptance angle, but rather to the largest range of orientations, measured relative to the sample surface normal, that could possibly be detected. It is made relevant since the distribution of emitted electrons goes as $\cos\theta$.

1.7 van Noort and van Gorkum DSCEMS Spectrometer

The spectrometer which is the topic of this thesis, is based on a design by van Noort and van Gorkum[24],. This design is shown in Figure 1.10, and is of the Retarding Field Analyzer (RFA) type as described by Huchital and Rigden[25], and Staib and Dinklage[26].

The functioning of the spectrometer is as follows. First, the γ-rays strike the sample releasing electrons which travel through a field free region to Grid 1 at ground potential. They then travel through Grid 2 at a negative potential, -V2, into the

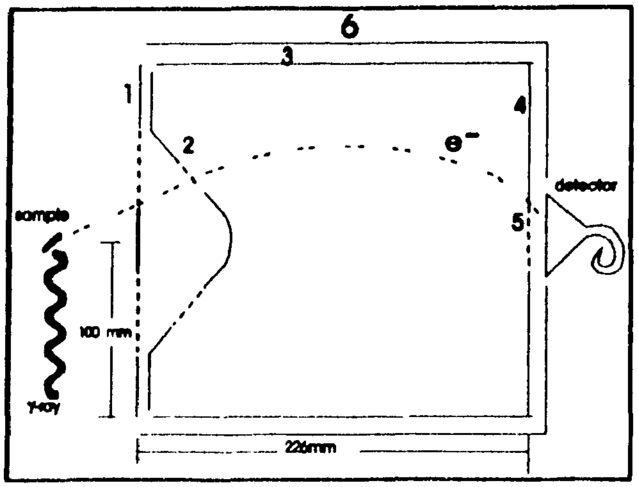

Figure 1.10 van Noort and van Gorkum Retarding Field Spectrometer

largest region of the spectrometer. Grids 3,4,and 5 are all at the same potential, -V1, which is negative relative to the potential on Grid 2. The configuration of the grids focuses electrons that are within a selected energy window of the pass energy, through Grid 5 into an extended channeltron detector. V1 determines the pass energy of the detector, while the ratio of V2/V1 determines the energy resolution.

All grids were constructed from 250μm stainless steel plate with holes burned in them with a Nd-YAG laser. Grid 1 and Grid 2 are 81% transparent while Grid 3, Grid 4, and Grid 5 are 93% transparent. Grid 6 is at ground potential and acts to collect electrons which travel through Grid 3. Grid 2 is cone shaped with a hemispherical top, and an extended flat base. Its purpose is to reduce spherical abberation so that larger samples may be employed. Its shape is a simplification of a spherical Bessel-function based on work presented in a paper by van Gorkum[27]. The combination of Grid 1 and Grid 2 determine the angular region over which the spectrometer functions as a energy selective detector.

The spectrometer has an energy resolution which may be varied from .1% and 5%. It has a luminosity of 3.9 mm² at a resolution of 2%. It is capable of detecting electrons emitted from the sample in almost any angular region by blocking off portions of grid 2. It is also capable of detecting electrons with energies up to 25 keV. A small tungsten filament allows for heating the sample up to temperatures of 1000 K. An elaborate cooling system allows for the acquisition of spectra from samples with temperatures as low as 25 K. The cooling system consists of a cold finger which makes good thermal contact with the sample holder, and a liquid nitrogen bath for the rest of the system to reduce heat input to the sample. The system is under UHV attained with an ion getter pump. This type of pump does not vibrate, so that the Mossbauer lines are not broadened. The ions produced by the getter pump did produce background counts from the detector, and a shield was required to reduce this background, at the expense of pumping speed. The system also has a sample transfer system so that samples may be changed without breaking vacuum, and an argon ion gun for in situ cleaning of the sample surface.

Chapter 2: Designing and Dimensioning the Spectrometer

2.1 Considerations in Choosing a Prototype and Necessary Eliminations from that Design

The primary characteristic that we desired for our spectrometer was high performance, and we hoped to attain this with a simple design. It was also important to build a spectrometer which had a flexible design, so that future improvements could be implemented as needs arose and resources became available. The spherical spectrometers required difficult construction, and lacked the flexibility in design that we desired. The choice was therefore narrowed between a magnetic type, a CMA type, and an RFA type. The magnetic spectrometers could quickly be eliminated since they did not improve upon the performance of the CMA, yet they introduced magnetic fields at the sample location. Though the CMA offered the most simple construction, its luminosity was slightly less than that of the RFA (at the same resolution) without a significant advantage in terms of its construction ease. The RFA design of van Noort, and van Gorkum was thus chosen.

Some of the features of the prototype were not necessary for our purposes. The prototype's ability to collect spectra from samples cooled to 25 K was considered unnecessary. Fortunately, the flexibility of the design meant that, in the future, temperatures close to 77 K could be reached with a simple cold finger making good thermal contact with the sample holder. The extra 52 K of cooling would not significantly improve the recoil free fraction, or increase the experimental possibilities of the spectrometer. Eliminating the 25 K feature also eliminates the effort involved in constructing a sample bath for the entire spectrometer, and the design difficulties involved in attaining Ultra High Vacuum [UHV]. UHV is required at very low temperatures since significant quantities of ice form on the sample if the pressure is not low enough. Liljequist[5] reports that at a vacuum of $5x10^{-8}$ torr, a 200-300 Å layer of ice formed on a sample at a temperature -100°C after a few hours.

In order to obtain UHV the prototype used an ion getter pump. This pump, though it produced background counts, was said to be necessary in order to eliminate mechanical vibrations. However, Sato and Mitsuhashi[28] report that a turbomolecular pump fitted directly to the vacuum chamber of their DSCEMS spectrometer produced no noticeable Mossbauer linewidth broadening. So long as the entire system vibrates as a single unit, broadening should not occur. A diffusion pump will introduce fewer vibrations than a turbomolecular pump, and hence, should be at least as effective. It was therefore decided to connect a diffusion pump directly to our chamber.

A further major difference between our spectrometer and the prototype, was in the methods employed to fabricate the grids. At Phillips Research laboratory where the prototype was built, access was available to laser machining. They were able to produce high precision, sturdy grids with excellent transmission properties, using laser drilled stainless steel foil. Though we did not have direct access to the laser machining methods, we were able to reproduce the characteristics of the grids using stainless steel mesh and photo-etched copper foil with processes that will be described in chapter 3.

The prototype spectrometer also used an extended channeltron detector, and this was replaced in our spectrometer with a microchannel plate [MCP] detector. The channeltron must be extended in order to obtain the detection area (diameter=40mm) required. The change to an MCP detector was implemented to avoid the difficult process for extending a channeltron. An extended channeltron is also very fragile. A description of the MCP, and a comparison of its performance to that of the channeltron, are given in sections 4.5 and 6.2 respectively.

2.2 Description of Computer Programs Written to Dimension and Analyze the Performance of the Spectrometer

Four computer programs were written for the purpose of finding the ultimate dimensions for the spectrometer, the acceptable tolerances for those dimensions, and the spectrometer performance characteristics. The first calculated the potentials within the spectrometer. The other three calculated electron trajectories in these potentials in order to plot a) energy resolution curves, b) electron trajectories, and c) phase space diagrams.

The cylindrical symmetry of the spectrometer allowed for a simplification of potential calculation, since the problem may be reduced to a 2-dimensional boundary value problem governed by Laplace's equation, $\nabla^2 V=0$. The two dimensional simplification is important because the computer memory required for a large 3-

dimensional grid is prohibitive, and unnecessary. Physically, the problem was solved by defining a grid in z and r, inputting boundary conditions, and then, using an iterative procedure to converge to the solution.

If all the boundary conditions were on grid points, one method of approaching a solution would be to take the properly weighted average of each grid point's nearest neighbours to be that grid point's new value, and then, iterate through the grid until the potentials converged. Unfortunately, the convergence is too slow to be useful. That is, the difference between the grid point values, and the weighted average of its nearest neighbours, becomes small compared to the difference between the grid point value and its converged value.

The slow convergence was overcome by the well known technique of Simultaneous Over Relaxation (SOR)[31]. This method takes as the new value for a grid point, 1-q (where q is a factor between 1 and 2) times the previous value of the grid point, plus the weighted average of the nearest neighbours multiplied by a factor of q. That is,

$$V^{new} = (1-q)\,V^{old} + qV^{weighted}. \qquad (2.1)$$

The factor, q, that promotes the fastest convergence of the potentials can be determined by trial and error. Its value depends primarily on the number of grid points in the system.

The weighting distribution of the grid points was accomplished by converting the governing partial differential equation into a difference equation. In cylindrical coordinates, Laplace's equation is,

$$u_{rr}+\frac{u_r}{r}+\frac{u_{\theta\theta}}{r^2}+u_{zz}=0 \qquad (2.2)$$

The partial derivative in θ can be eliminated due to the cylindrical symmetry, and then the equation can be solved for V by assuming that the distance, d, between grid points, is small enough that,

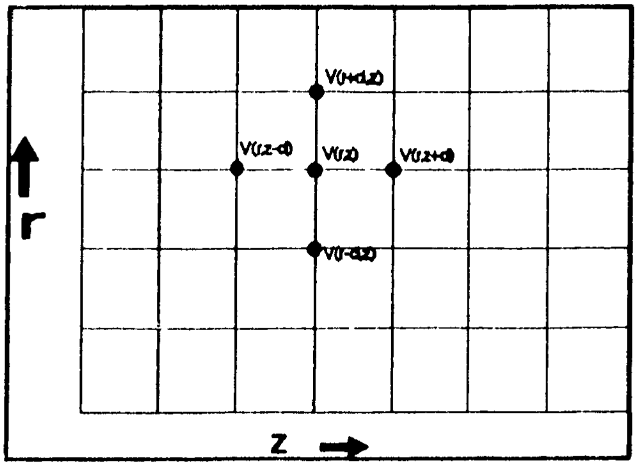

Figure 2.1 Finding Finite Difference Derivatives in Cylindrical Geometry

$$\frac{\delta V}{\delta r}\approx\frac{\Delta V}{\Delta r} \text{ and } \frac{\delta V}{\delta z}\approx\frac{\Delta V}{\Delta z} \qquad (2.3)$$

This implies (see Figure 2.1), that

$$\frac{\delta V}{\delta r}=\frac{1}{2d}\left(V(r+d,z)-V(r-d,z)\right) \qquad (2.4)$$

$$\frac{\delta^2 V}{\delta r^2}=\frac{1}{d^2}\left[\left(V(r+d,z)-V(r,z)\right)-\left(V(r,z)-V(r-d,z)\right)\right] \qquad (2.5)$$

$$\frac{\delta^2 V}{\delta z^2}=\frac{1}{d^2}\left[\left(V(r,z+d)-V(r,z)\right)-\left(V(r,z)-V(r,z-d)\right)\right] \qquad (2.6)$$

The equations for the derivatives (2.4), (2.5), and (2.6), were then substituted back into Laplace's equation. The result was rearranged to obtain an equation for V(r,z), where V(r,z) represents the weighted average of the nearest neighbours as previously described. We obtained,

$$V(r,z) = \frac{1}{4}\left(V(r,z+d) + V(r,z-d)\right) + \frac{1}{8r}\left[(2r-1)\,V(r-d,z) + (2r+1)\,V(r+d,z)\right] \tag{2.7}$$

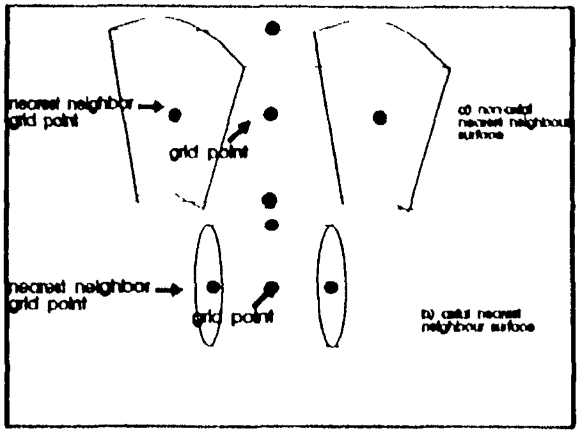

Figure 2.2 Nearest Neighbour Regions Formed by Grid Points

Different weighting equations are required for axis points and points adjacent to the cone boundary. A visual description is helpful for understanding the weighting of the grid points. The potential at the geometric centre for any Laplacian region is given by the average of the potential on the surface enclosing the region(Mean Value Theorem [MVT][29]). Each grid point is the geometric centre of a region wherein the surfaces enclosing that region contain nearest neighbour grid points, and lie upon values of constant r or z (see Figure 2.2). We define the surface of that region to be the Nearest Neighbour Surface [NNS].

For points along the axis, the NNS will be a cylinder. The ends of the cylinder will have an average potential on them given by the potentials of the axial nearest neighbour grid points (assuming a linear field variation between grid points). The curved cylindrical portion will have an average potential given by the nearest neighbour in the radial direction (also assuming linear variation). The weighting of the three nearest neighbours, representative of the two ends and the curved portion, will be given by the ratio of the areas of the ends to the curved portion in order to satisfy the MVT. The result is,

$$V(0,z)=\frac{2}{3}V(d,z)+\frac{1}{6}V(0,z-d)+\frac{1}{6}V(0,z+d) \qquad (2.8)$$

For points that are bordering a boundary which is itself not attached to a grid point (i.e. the cone boundary), new weighting factors must be developed. The weighting factors are calculated by replacing the nearest neighbours that lie across the cone boundary, with the points (see Figure 2.3) where the boundary curve intersects the horizontal and vertical lines through (r,z). A new NNS will thereby be formed in which, the boundary imposed nearest neighbours will have the fixed potential V2. The substitution of a nearest neighbour grid point for a boundary point changes the NNS in two ways. It moves the geometric centre away from the grid point, and it changes the ratio of the total area of the constant z surfaces, in comparison to the total area of the constant r surfaces.

The method for obtaining the weighting coefficients will now be shown in detail, for the case in which the grid point lies on the detector side of the cone boundary, and within a single grid spacing in both dimensions of the that boundary. The weighting equation must take the form,

$$V(r,z) = aV(r,z+d) + bV2 + cV(r+d,z) + dV2 \qquad (2.9)$$

where a,b,c,d are the weighting coefficients. Normalization requires that a+b+c+d=1. The ratio a/b, must equal $1/a_z$, to reflect the ratio of the axial distances from the grid point to the actual nearest neighbour as compared to the nearest neighbour

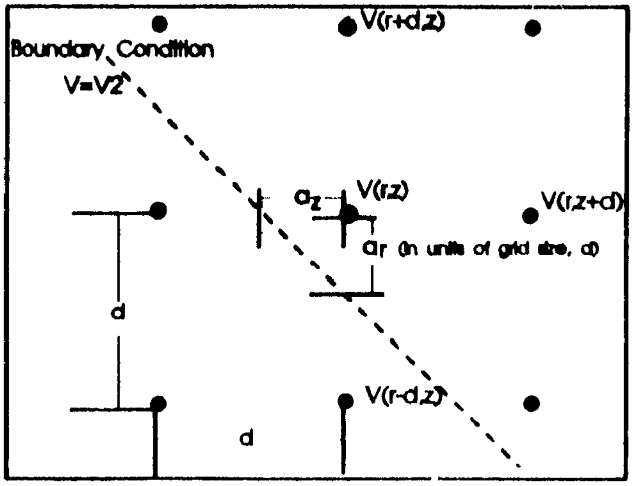

Figure 2.3 Calculating Weighting for Points Adjacent to the Boundary of the Cone (dotted line)

defined by the boundary. The ratio c/d, must equal (2r-1)/[(2r+1)a_r] to reflect both the radial surface area proportions (from (2.7)), and the radial nearest neighbour distance proportions from the grid point. The ratio of (c+d)/(a+b) is equal to (1+a_r)/(1+a_z). This ratio reflects changes in the proportions, of the total radial surface area, as compared to the total constant z surface area, created by the change in the NNS. We thus have four equations in four unknowns,

$$a + b + c + d = 1 \tag{2.10}$$

$$\frac{a}{b} = \frac{1}{a_z} \tag{2.11}$$

$$\frac{c}{d} = \frac{2r-1}{a_r(2r+1)} \tag{2.12}$$

$$\frac{c+d}{a+b} = \frac{1+a_r}{1+a_z} \tag{2.13}$$

Solving the system of equations we obtain,

$$a = \frac{1}{2+a_r+a_z} \tag{2.14}$$

$$b = \frac{a_z}{2+a_r+a_z} \tag{2.15}$$

$$c = \frac{1+a_r}{2+a_r+a_z}\,\frac{2r-1}{2r-1+a_r(2r+1)} \tag{2.16}$$

$$d = \frac{a_r(1+a_r)}{2+a_r+a_z}\,\frac{2r+1}{2r-1+a_r(2r+1)} \tag{2.17}$$

Similar expressions were found for conditions such as grid points with only one nearest neighbour intercepted by the cone boundary, and, grid points which are below the cone boundary rather than above it. A set of weighting expressions were thus found which could iterate any point on the two dimensional grid.

For the point of classification, there were four different categories of points which required updating in different manners. These are perimeter points, interior points, axis points, and border points. Perimeter points are those on the cylinder or its ends, and their values are fixed by the boundary conditions. Interior points are those points that do not lie on the axis of the cylinder, and are not separated from their nearest neighbours by a defined boundary condition (namely those imposed by the cone), and must be updated according to (2.7). Axis points lie along the axis of the cylinder, and are updated according to (2.8). Border points are those which border the cone. The coefficients of border points must be calculated as was described above to obtain the coefficients. Eight sets of coefficients will be required since there are eight possible ways in which a border point may be configured.

It now remains to give some further detail as to the technique employed for obtaining an acceptably fast convergence of the iteration procedure. As was previously mentioned, a parameter q must be found which will accelerate the convergence. Our particular problem required two q values since there are two enclosed regions, the region inside the cone, and the region between the cone and the cylinder. The expression to determine q in a cylindrical region is,

$$q = \frac{2}{1+\sqrt{1-\frac{1}{4}\left[\cos\left(\frac{\pi}{Ld}\right)+\cos\left(\frac{\pi}{Rd}\right)\right]^{2}}} \qquad (2.18)$$

where L and R are respectively the axial and radial lengths of the cylinder, and d is the grid spacing[30]. This expression is not directly applicable to the uniquely shaped regions of the spectrometer, but was used to provide reasonable starting points for the q values.

The approximations were found by choosing a cylinder which has the same average length and average radius as the cone region. The first q value was calculated based on this cylinder. The second q value was calculated based on a cylinder defined as having the same volume as, the full spectrometer cylinder less the volume enclosed by the cone, but with the radius and length in the same ratio as that of the full cylinder. These initial guesses were then used by a version of the potential configuration program which focused in on the values of q which led to the fastest convergence. The focusing was accomplished by determining the two q values that led to the most accurate value of the potential at two grid points, chosen near the centre of their respective regions, after a set number (~100) of sweeps through the grid had been performed.

Since the ultimate purpose of the programs is to determine the sensitivity of the performance of the spectrometer to the critical dimensions of the apparatus, the q values should in principle be recalculated each time the dimensions of the spectrometer change. In our case though, a 1 mm grid size was employed so that our mesh size was approximately 225x100. We were interested in dimensional changes of at most 2 millimetres, since there would not be any technical difficulties obtaining such large tolerances in the fabrication of the device. As the literature[31] shows that it is best to choose q values which are slightly larger, rather than slightly smaller than the true value, we added .005 to the determined q values (q~1.75). It was found that convergence was not significantly altered for the small dimensional changes tested, and hence, it was not necessary to make a separate calculation of q each time that a spectrometer dimension was altered. We note that it is the large region (the region that excludes the cone) that determines the ultimate number of iterations needed, since it contains more grid points. This means that the size of the dimensional changes need only be compared to this larger volume.

It is a crucial fact to realize, and one often not mentioned in the literature, that the asymptotic rate of convergence for a particular q value is not obtained until the number of iterations through the entire system is approximately equal to the number of grid points in the largest dimension of the system. The error often grows by a factor of 20 before convergence sets in. This meant that, when we input the boundary conditions, set the rest of the grid points to zero potential, and began our iterations with our determined q values, the potentials diverged. In regular, cylindrical and rectangular coordinates, this is overcome by the use of the Chebyshev acceleration technique[31]. Unfortunately, the formulas for the advancement of the q value in Chebyshev acceleration are very difficult to obtain analytically for non-cylindrical regions. It is theoretically possible to make an adequate estimation using the same ideas as were employed in finding the initial q values, but as we had access to fast computers, Chebyshev acceleration was not particularly advantageous. It was found that by making approximately 300 iterations through the entire mesh with $q=0$, and then switching to the determined q values, asymptotic convergence was obtained. It should also be noted that a set of five standardized potential configurations where stored in memory and used as starting points for similar configurations, and it was not necessary to perform more than 100 initial iterations from these starting points in order to achieve successful convergence.

Another useful technique for the problem at hand was to process the mesh points in an alternating fashion. If the mesh is divided into odd and even points, like a chess board is divided into black and white squares, then an odd point will only have even nearest neighbours and vice versa. We were able to halve the number of iterations by performing half sweeps, wherein only odd or even points are updated. The process is commonly referred to in the literature[31].

The electron trajectories were calculated by assuming linear variations in the potential between planes perpendicular to the axis that pass through neighbouring grid points. This implies that there will be a constant force on the electrons as they travel between the planes perpendicular to the walls of the cylinder which intersect grid points. A constant averaged field was calculated for the electron each time it passed one of these planes, and then by integrating to the next plane, the subsequent position of the electron was found. This procedure was repeated so that the full trajectory of the electron was traced out.

This method is not valid for electrons which are travelling in a direction nearly perpendicular to the walls of the cylinder, since they may travel several radial grid spaces before reaching the next plane, and the potential can not be assumed to be constant over such large distances. However, the only electrons that could strike the detector after attaining an orientation of more than 45° are those near the detector entrance, since all others will not have enough momentum in the direction parallel to the axis of the spectrometer to overcome the strong repulsion from the backplate. It was verified that even at the highest useful resolution setting (V2/V1=.85), where the fields are most non-linear, an electron with an orientation of 64° would not see more than an 11% change in the radial force due to non-linear terms. Since the repulsive axial force is nearly 100 times stronger than the radial force near the detector entrance, the electron trajectories bend away from the detector very rapidly once the orientation angle becomes greater than ~45°. Trials with the program revealed that at highest resolution not more than 3% of electrons that struck the backplate within 10 mm of the detector, had an angle of incidence of more than 64°. Our simplified method of finding electron trajectories was thus suitable for the purpose of evaluating electron performance.

2.3 The Use of the Trajectory Calculating Programs

2.3a) Dimensions, Tolerances, and Effects of Physical Defects

Resolution curves represent the count rate of detected electrons as a function of the energy of those electrons before entering the spectrometer (the pass energy). The width of the curves represents the pass band that the spectrometer selects, and the height of the curves is a measure of the spectrometer's efficiency. Resolution curves are the most direct evaluation of spectrometer performance.

The simulated electron emission distributions used to determine the height of the resolution curves at a particular energy had to reflect the actual distribution from a real three dimensional sample orientated at 45° to the axis of the spectrometer. In our two dimensional simulations, an isotropic distribution from a sample orientated at 90° to the axis was used, and found to be both, simple to carry out and in agreement with the simulations by van Noort and van Gorkum who reported that their three dimensional simulations showed an insignificant change in the transmission characteristics when the sample is placed at 45°[1].

In order to test the effects of dimensional changes, resolution curves were produced corresponding to small increases and decreases in all of the dimensions of the spectrometer. The spectrometer resolution was maximized (.8%) in producing these curves so that the effects on the performance of the spectrometer would be most obvious.

The physical meaning of the dimensional variables is shown in Figure 2.4, and Table 2.1 lists their value, and their tolerance. The tolerances were calculated as the amount of change in a variable that would produce a 5% decrease in the number of detected electrons at the pass energy, or for insensitive variables a tolerance is stated which will be technically easy to attain. If the dimensional change decreased the resolution, the number of detected electrons at the pass energy was assumed to be smaller by the fraction that the resolution decreased. Owing to the fact that there is a large variation in the manner in which the resolution curves are affected, comments are included.

The tolerances show that the spectrometer is not so sensitive to dimensional changes as to discourage construction. In

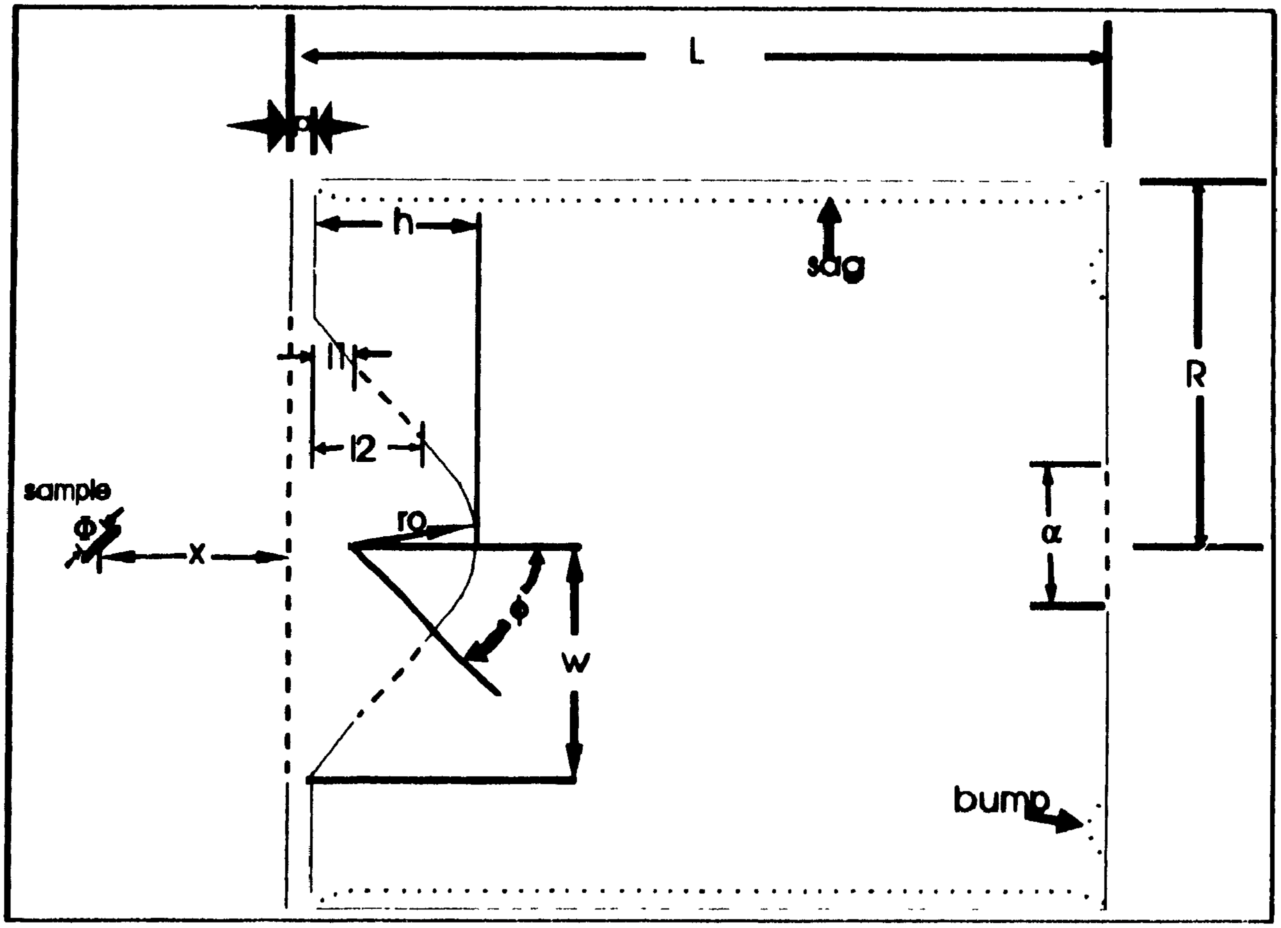

Figure 2.4 Variables Employed for Dimensioning the Spectrometer

particular, the suggestion by the builders of the prototype that the shape of the cone should have a tolerance of not more than .1 mm, is not supported by our simulations.

The dotted lines in Figure 2.4 are representative of two physical defects that we were unable to avoid in the construction of the spectrometer. That referred to as 'sag' corresponds to the tendency of the cylindrical mesh to be pulled inwards due to uneven tension on the mesh. Though our simulations could only represent an axially symmetric 'sag', the effects should be of the same magnitude. The term 'bump' corresponds to a deviation in the backplate of the spectrometer, created by the conductive epoxy contact made there. Once again, only an axially symmetric 'bump' could be tested. No significant changes were found in the spectrometer's performance due to these defects.

The distance 'p' was required in order to ensure adequate insulation between the grids. Since our grids were not as smooth as the prototype's, greater distances between the grids were necessary.

A further difference between our spectrometer and the prototype, was that our acceptance angle was determined by the size of the transparent portion of the focusing lens, whereas the acceptance angle of the van Noort et. al. spectrometer was determined with an interchangeable entrance aperture. The change was implemented so that a smaller area needed to be etched from the focusing lens, and hence, our etching success rate would be higher, and the lens would be sturdier. There was concern that at broader resolution settings, the potential on the cone would change the orientations of incoming electrons, thus changing the location on the cone that should be transparent for maximum performance. Tests showed that this was not the case, which is consistent with the fact that the electrons approach the transparent area of the cone at near perpendicular angles to it.

Table 2.1 Spectrometer Dimensions and Tolerances

Variable	Δ	Intensity Decrease for +Δ	Intensity Decrease for -Δ	Optimum Dimension and Tolerance	Comments
L	2mm	<.5%	<.5%	226±2 mm	insensitive
R	2mm	3%	2%	100±2 mm	intensity increase and resolution broadening as R increases
h	1mm	<.5%	<.5%	19±1mm	Shift to higher pass energy as h decreased, but little change in resolution curve
ro	1mm	<.5%	<.5%	30±1mm	insensitive
Ø	2°	<.5%	<.5%	45±2°	insensitive
w	1mm	<.5%	6.5%	62.5±.8 mm	decrease in w causes intensity increase and resolution broadening
l1	2mm	<.5%	<.5%	15±2mm	electrons do not strike detector from these orientations
l2	1mm	3.8%	-4%	29±1mm	increasing l2 creates tail on hard side of resolution curve so that the increase of 4% is deceiving
p	1mm	6.5%	<.5%	3±.75mm	decreasing p cuts off some of the higher energy electrons

Variable	Δ	Intensity[i] Decrease for +Δ	Intensity[i] Decrease for −Δ	Optimum Dimension and Tolerance[ii]	Comments
X	1mm	6%	<.5%	50±.8 mm	decrease in X results in sharper orientation distribution
Φ	2mm	12%	-2%	10±.8 mm	decreasing sample size narrows resolution at expense of count rate
12-11	2mm	3.8%	-4%	14±2 mm	same effect as increasing 12 by 1 mm
α	2mm	18%	12%	10±.55 mm	resolution curve broadens quickly for increased diameters
sag[iii]		3%			Equivalent to decreasing R
bump[iv]		1%			insensitive

---

[i] In cases where the resolution changes, the intensity (height of resolution curve) is adjusted by scaling the curve to .8% resolution. This method is inadequate if a tail is produced in the curve such as when 12 is increased.

[ii] In those cases in which the intensity change is less than 2.5%, the tolerance is assigned a value which is technically easy to attain, otherwise the tolerance is calculated based on the change in a dimension which would produce a 5% decrease in the intensity (see [i]).

[iii] The sag corresponded to a 2 mm decrease in R along the cylinder from the 10th to the 216 mm.

[iv] The bump was 2 mm high, 2 mm long, and located 75 mm from the axis of the cylinder

2.3b) Predicted Performance Characteristics of the Spectrometer

Figure 2.5 shows the minimum, maximum, and three other resolution curves, for the chosen spectrometer dimensions. The height of the curves is a measure of the fraction of accepted electrons (electrons with trajectories that trace through the transparent portion of the cone) that strike the detector. This fraction is referred to as the striking fraction. The horizontal scale is a measure of the fraction of the pass energy that the potential V1 corresponds to. That is V1 (in volts) should be set to the horizontal position of the peak, multiplied by the desired pass energy (in electron volts). Since the pass energy is always within 5% of the corresponding setting of V1, the width of the curves is an accurate representation of the resolution, which is normally defined in terms of the pass energy.

Using the full width at half maximum criterion, the narrowest resolution of the spectrometer is predicted to be .8%, and the broadest resolution of the spectrometer is predicted to be 4.3%. At .8% resolution the striking fraction is .43, and at 4.3% resolution the striking fraction is .85. The detection count rate could therefore be expected to drop by a factor of nearly 11 (.85/.43x4.3/.8) in changing from narrowest to broadest resolution.

The spread in the location of the peaks indicates that the potential V1 will have to be adjusted with the resolution. (Note that the resolution is determined by V2/V1.) To that end, the values in Table 2.2 have been calculated for determining V1 at a desired resolution. For instance, to select 7.3 keV electrons within a 4.3% pass band, V1 should be set to .94x7300 volts, and V2 should be set to 0xV1 volts.

Table 2.2 Spectrometer Potential Settings

Resolution (percent of pass energy)	V1 (fraction of pass energy)	V2/V1
4.3	.94	0
3.5	.951	.21
3.0	.96	.31
2.5	.969	.40
2.1	.975	.49
1.5	.98	.70
1.0	.99	.82
.8	.992	.87

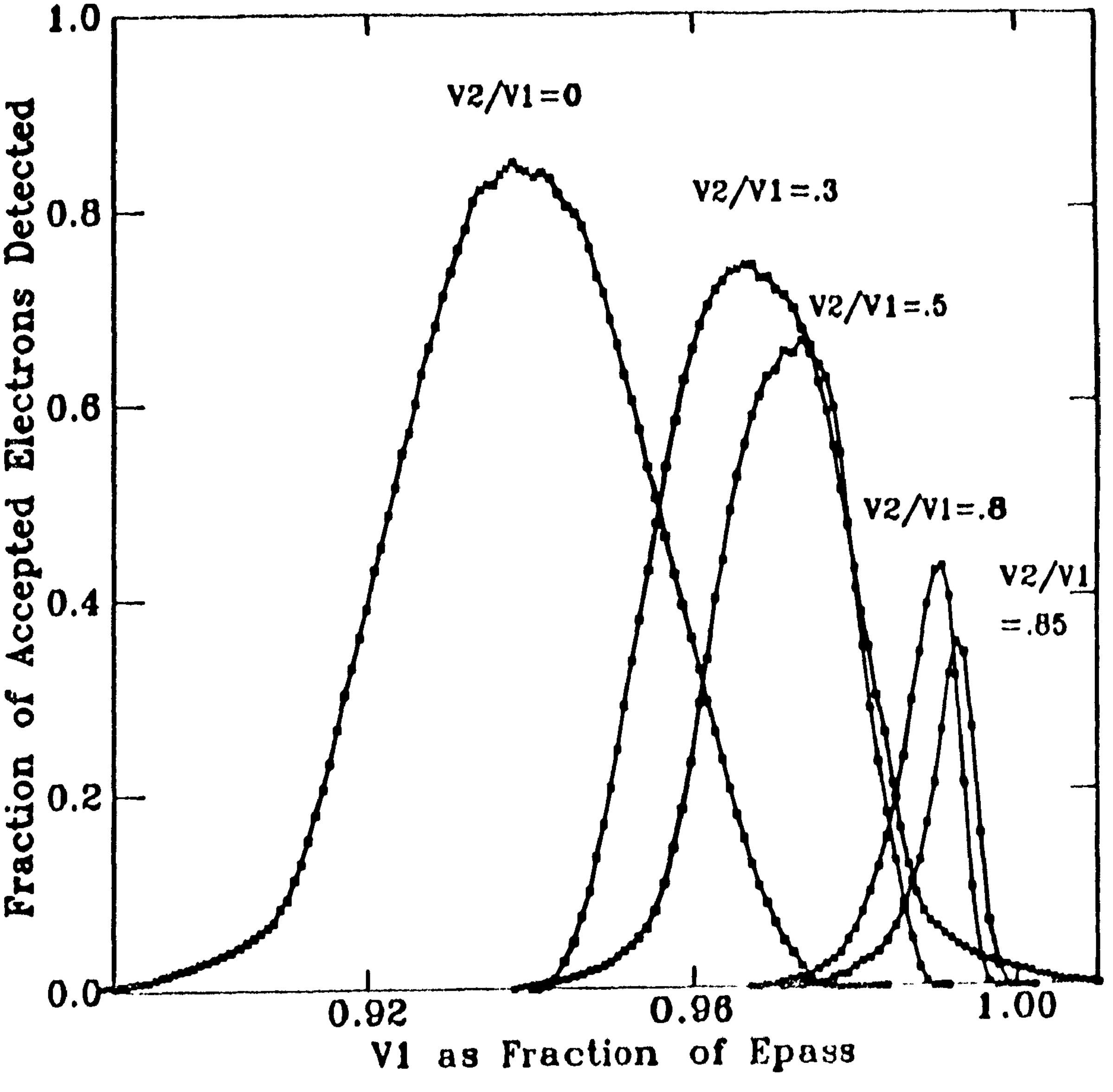

Figure 2.5 Resolution Curves for Full Range of Resolution Settings

2.3c) Plots of Electrons Trajectories

Figure 2.6 shows three sets of mono-energetic electron trajectories. It displays the ability of the spectrometer to discriminate between pass energy electrons, and electrons 2% above and below the pass energy. The resolution is set for 2.1%. In the top diagram where the incoming electrons have energy 1.02xEpass, the electrons strike above the detector. In the bottom diagram the electrons have energy .98xEpass, and so they fall short of the detector.

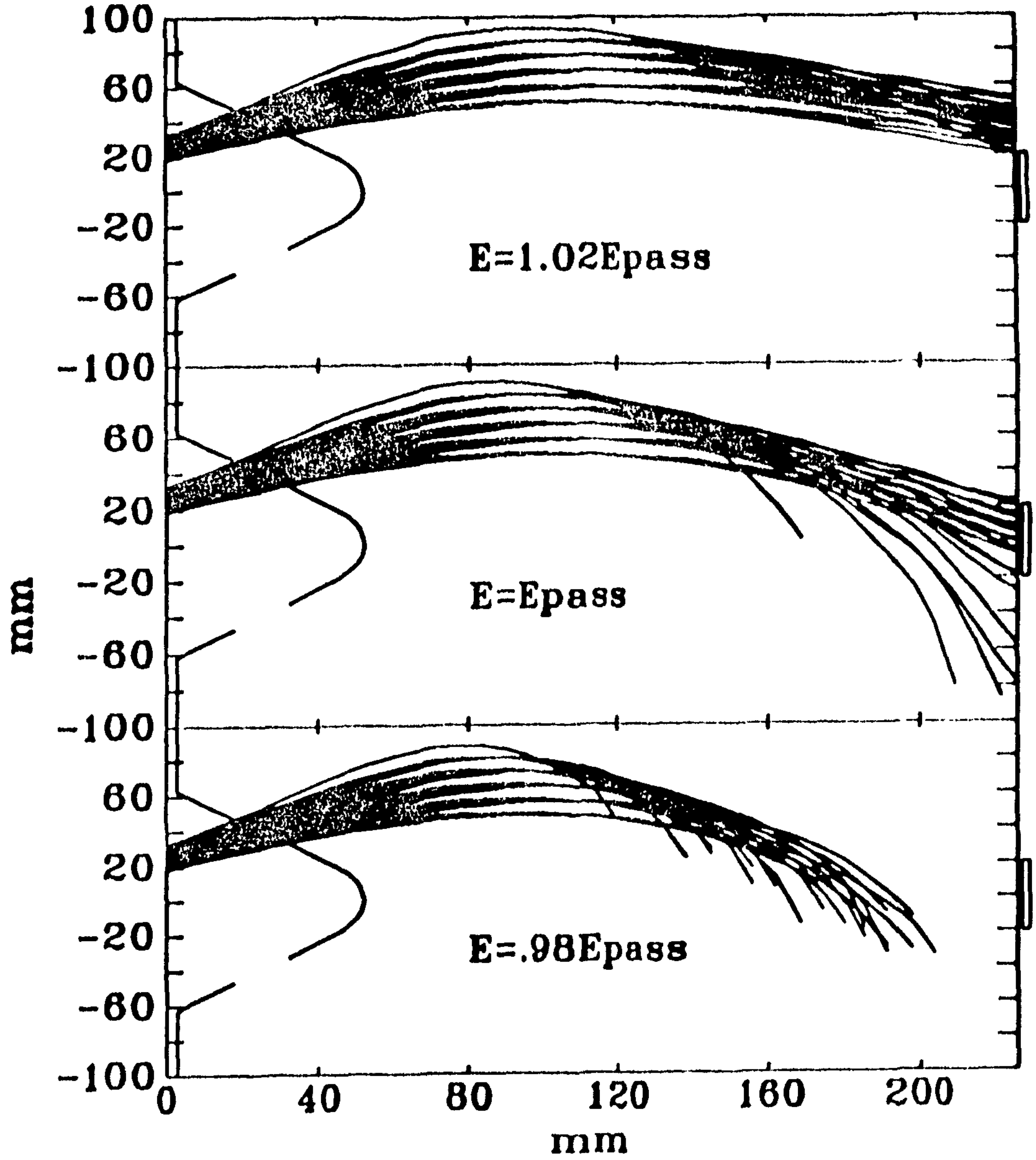

Figure 2.6 Electron Trajectories for Electrons of Energies, 1.02Epass, Epass, and .98Epass, and a Resolution Setting of 2.1%

2.3e) Phase Space Diagram

Phase space diagrams are shown in Figure 2.7. The diagrams, like the trajectory plots, were for mono-energetic electrons, and were calculated based-on a resolution setting of 2.1%. The horizontal axis represents the radial distance at which accepted electrons strike the backplate, and the vertical axis represents the arcsine of the angle at which the electrons strike the backplate. The two vertical lines represent the limits of the detector area. Points falling within these lines correspond to electrons that would be detected (if not blocked by the solid regions in the focusing lens). The data points originate from electrons that were released from the extremities of the 10 mm diameter sample so that the region within the data lines is representative of electrons emitted from a 10 mm diameter sample. The shaded regions correspond to detected electrons. This region should be maximized at the pass energy (middle diagram), and minimized at the limits of the passband (upper and lower diagrams).

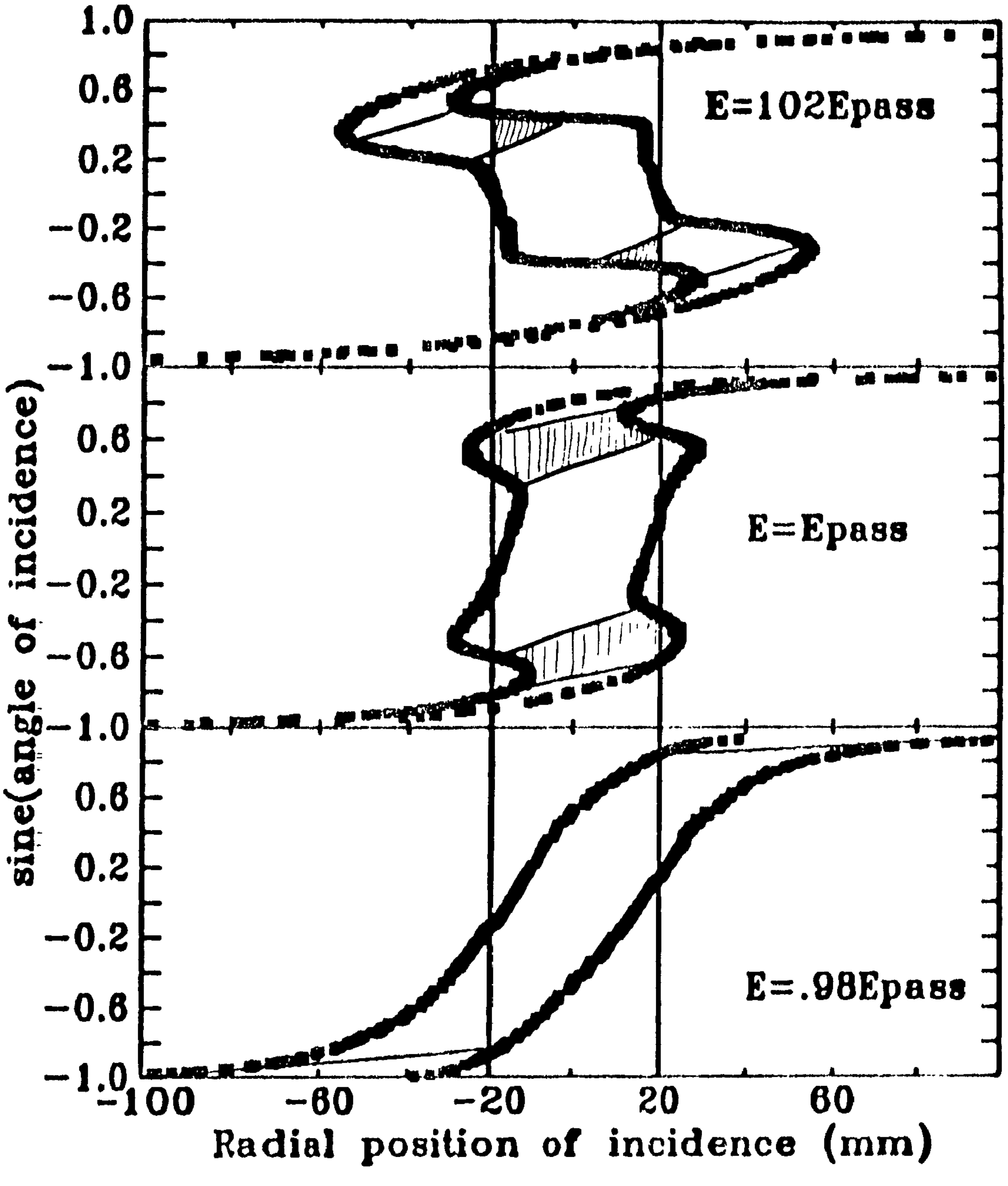

Figure 2.7 Phase Space Diagrams

Chapter 3: Construction and Assembly

3.1 External Assembly

Figure 3.1 is a photograph of the apparatus. Its basic components are the vacuum chamber, the pumping system, the table, the controls, and the transducer track.

The vacuum chamber is made from aluminum, chosen for low density, easy machining and welding. The chamber is securely bolted to the table which is also aluminum. The lid, and bottom of the chamber can be removed. The bottom carries the vacuum port on which the diffusion pump hangs.

Access to the internal assembly is had by removing the diffusion pump, and lifting the full chamber out of the table. At this point the lid may be removed, and then the cylindrical portion of the chamber can be lifted over the internal parts. What remains is the grid system and its wiring supported on the bottom portion of the chamber. The wiring is fed through high voltage, vacuum compatible, commercial connectors ("W.W. Fischer S.A.", model # 104A049 and 105A049)[32] on the bottom portion.

The lid of the chamber has welded in the centre of it, the sample cylinder. This cylinder has one beryllium window on each side of it so that γ-rays from the source can be transmitted through the cylinder without absorbing the rays. There is a port on the top which is fitted with a standard 3" diameter flange. A threaded disc has been welded to the bottom of the flange so that a sample mount can be attached.

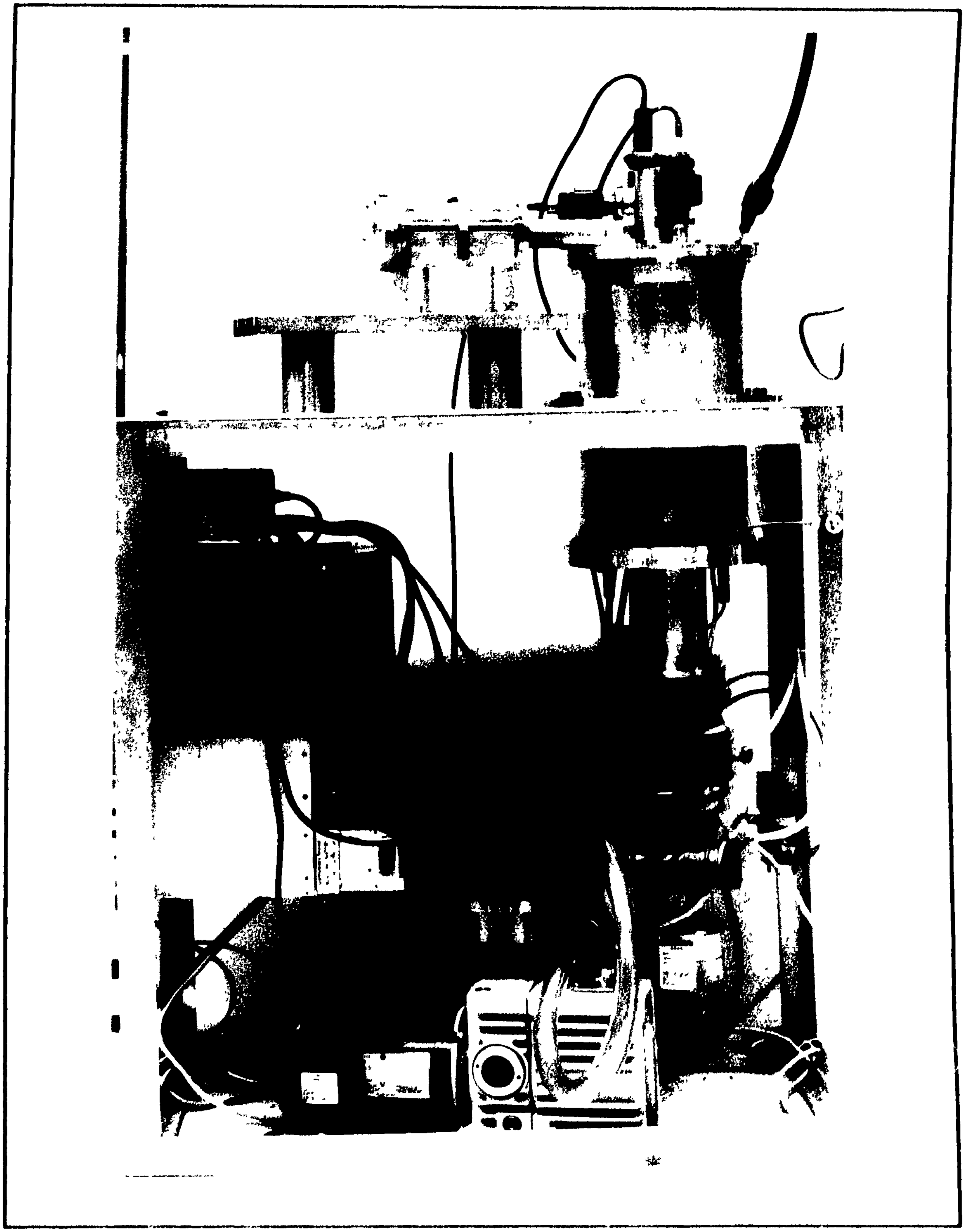

Figure 3.1 Photograph of the Apparatus

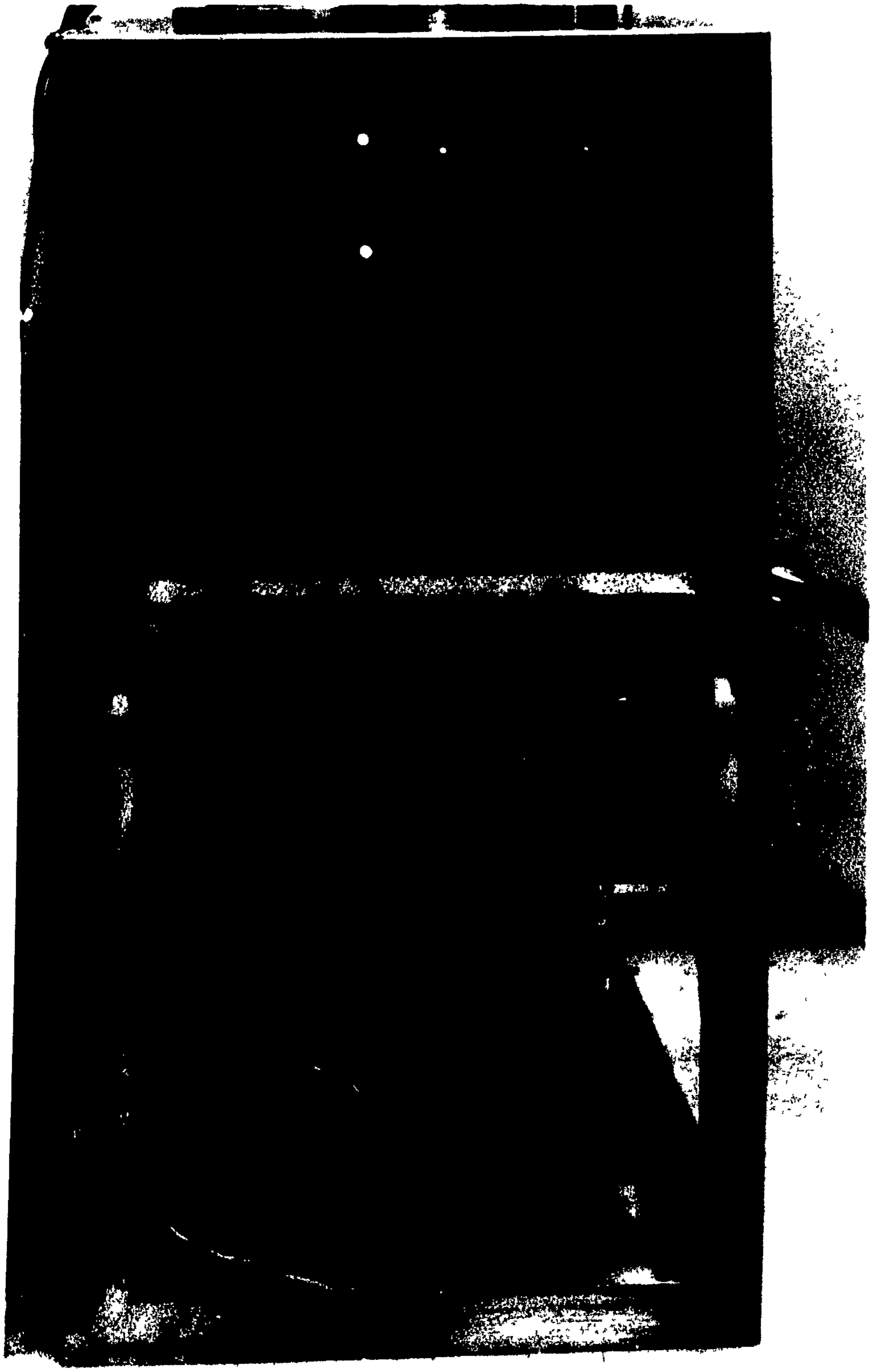

Figure 3.2 Photograph of Control Panel

The controls for the voltages, vacuum system, transducer, and detection amplification system, are mounted on the table (see Figure 3.2). The transducer track is supported on large aluminum legs, and is securely bolted to both the track and the table so that the entire system will vibrate as a single unit (see Figure 3.3). The track is of aluminum construction, and contains groves so the transducer can be moved without changing the alignment.

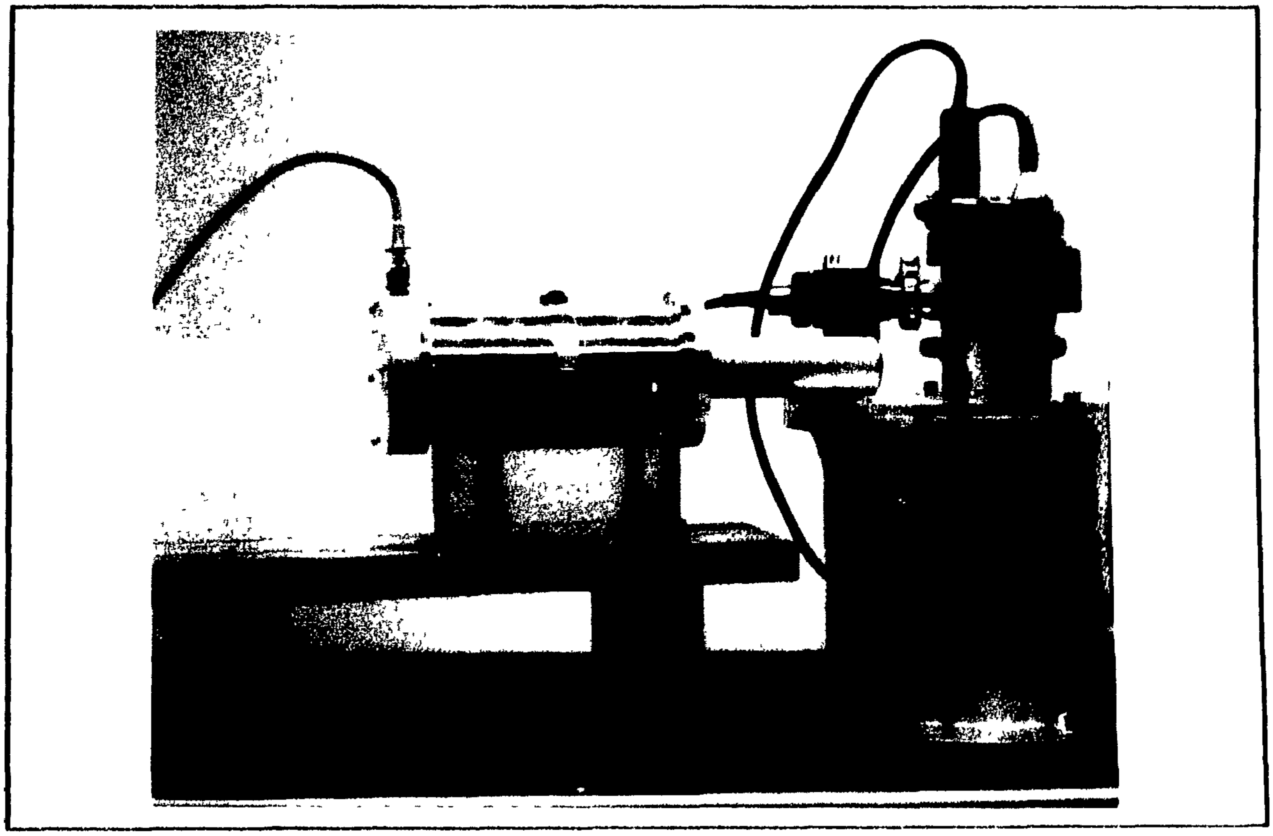

Figure 3.3 Photograph of Transducer Set-up

3.2 Internal Assembly

The internal assembly, as shown in Figure 3.4, consists of the foreplate, the canister, support rods, the detector mount and microchannel plate (MCP) detector, and the sample holder.

A cross sectional diagram of the foreplate is shown in Figure 3.5. It contains no detachable parts. The components of the foreplate are held together with Araldite[33], an epoxy with a low outgassing rate. Electrical contact between the top aluminum ring and the stainless steel mesh, and between the bottom aluminum ring and the cone, is made with a conductive (carbon filled) epoxy[34].

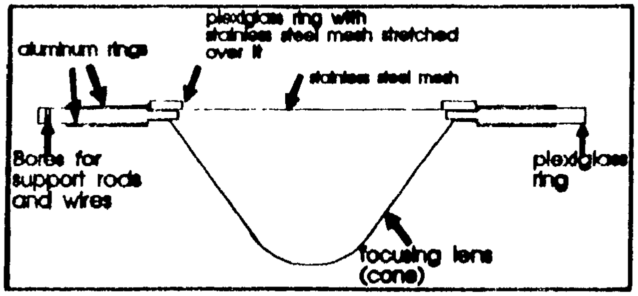

Figure 3.5 Cross Sectional View of the foreplate assembly.

The 'canister' assembly consists of a plexiglass ring, a plexiglass plate, and a cylindrical stainless steel mesh with 90% transmission. The mesh is glued to ridges on the ring and plate. Though not shown in Figure 3.6, there are eight aluminum support rods which extend through the large bores, and act to support the top ring and tension the mesh. There are also three delrin support rods which three of the aluminum support

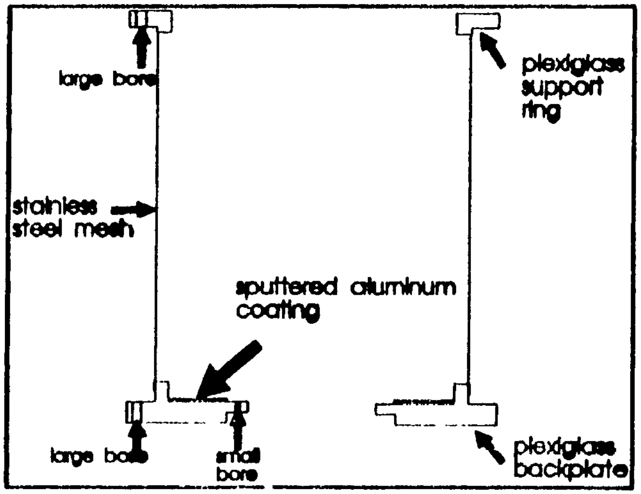

Figure 3.6 Cross Sectional View of the 'canister' assembly

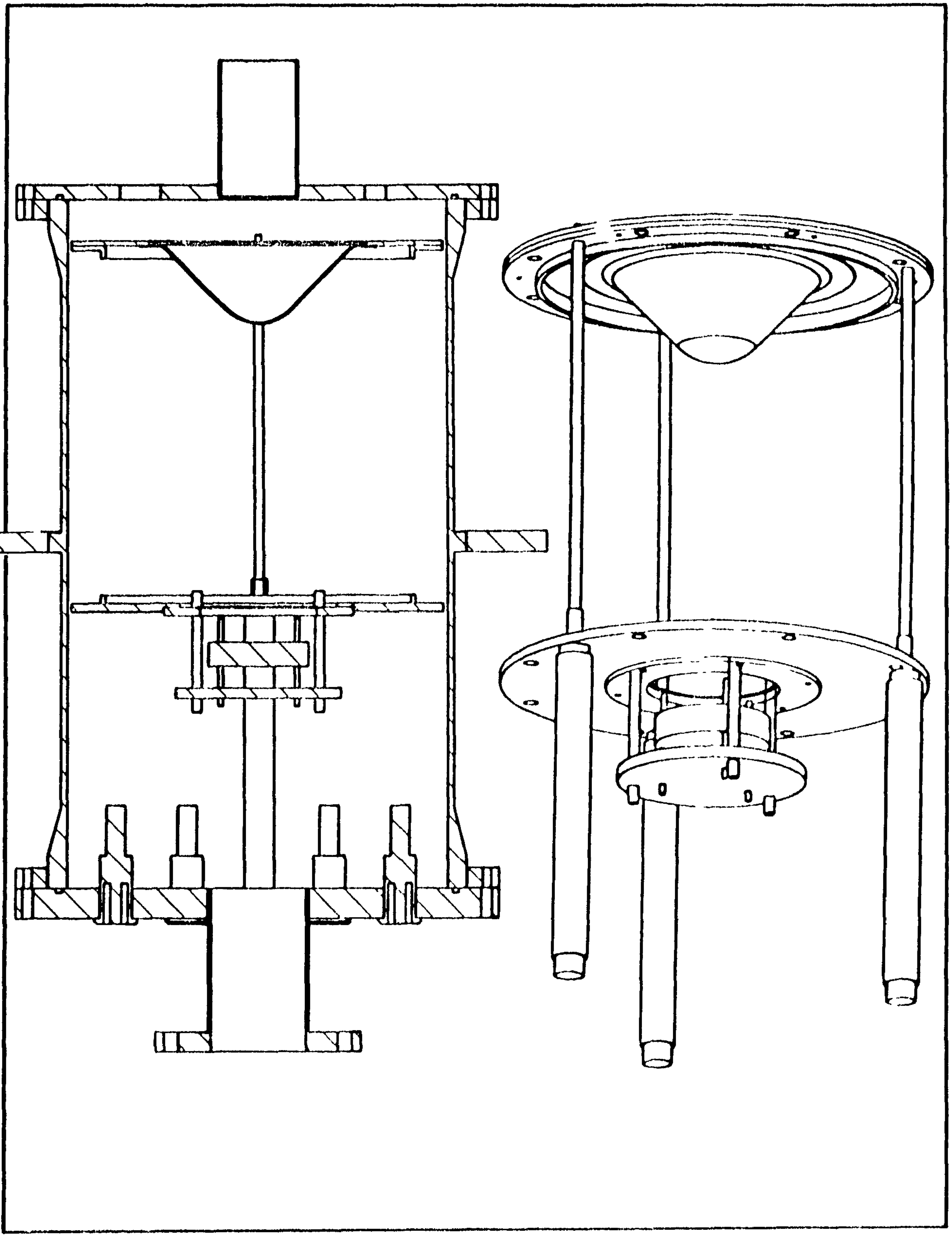

Figure 3.4 The Internal Assembly

rods may be screwed into, thereby holding the 'canister' above the bottom plate of the vacuum chamber.

If we begin from the top in Figure 3.7, depicting the MCP detector mount assembly, there is a thick (6 mm) plexiglass ring with the entrance mesh glued to the upward side of it. Nylon screws hold it into a depression in the back plate of the canister. The primary purpose of the ring is to support the rest of the detector mount assembly. On the detector side of the ring, three threaded nylon support rods fasten, so that the rest of the detector assembly, as a unit, can be slid over the rods, and held in place with nylon nuts. The MCP detector consists of two, .5 mm thick, 50 mm diameter disks, sandwiched together. Its operation will be described in the section 4.5. The detector rests in a depressed cavity inside the two plexiglass disks. The 3 mm thick disks have aluminum sputtered on the depressed rings for electrical contact with the MCP. There is also a 2 mm wide and 2 mm deep channel for wires on each disk. The channels are coated with aluminum, and lead to the detector contacts.

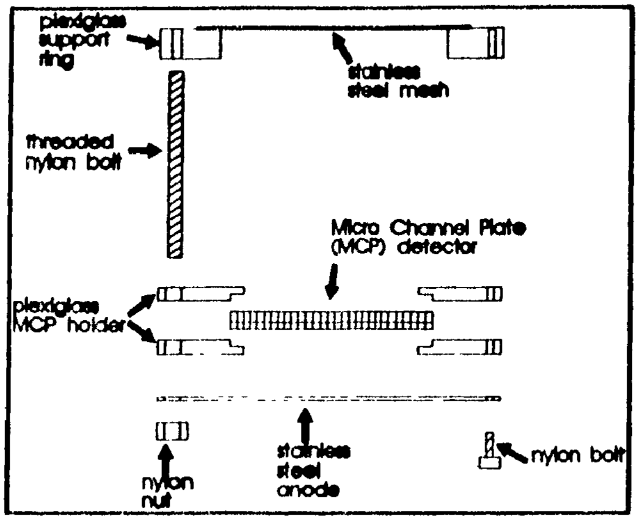

Figure 3.7 Cross Section of Detector Mount Assembly

The sample mount assembly (see Figure 3.8, and Figure 3.9), consists of an aluminum shaft, and a small elliptical ring that holds the sample to the shaft. The shaft has a threaded lead on the top of it which attaches to the external flange. The other end of the shaft is bevelled at 45°, and has a 20 mm diameter horizontal bore through the centre of the bevelled portion. The bore allows the incident γ-rays to exit the spectrometer, and the 45° bevelling represents a compromise between maximizing the amount of flux through the sample, and obtaining a sample orientation which will maximize the number of detectable electrons (i.e. there are more perpendicular emissions than glancing angle emissions).

Figure 3.9 Photograph of Sample Mount

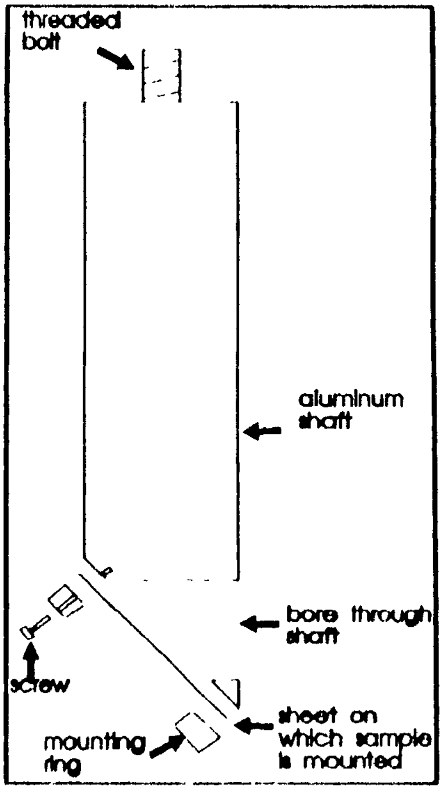

Figure 3.8 Cross Section of Sample Mount Assembly

3.3 Shaping and Etching the Focusing Lens

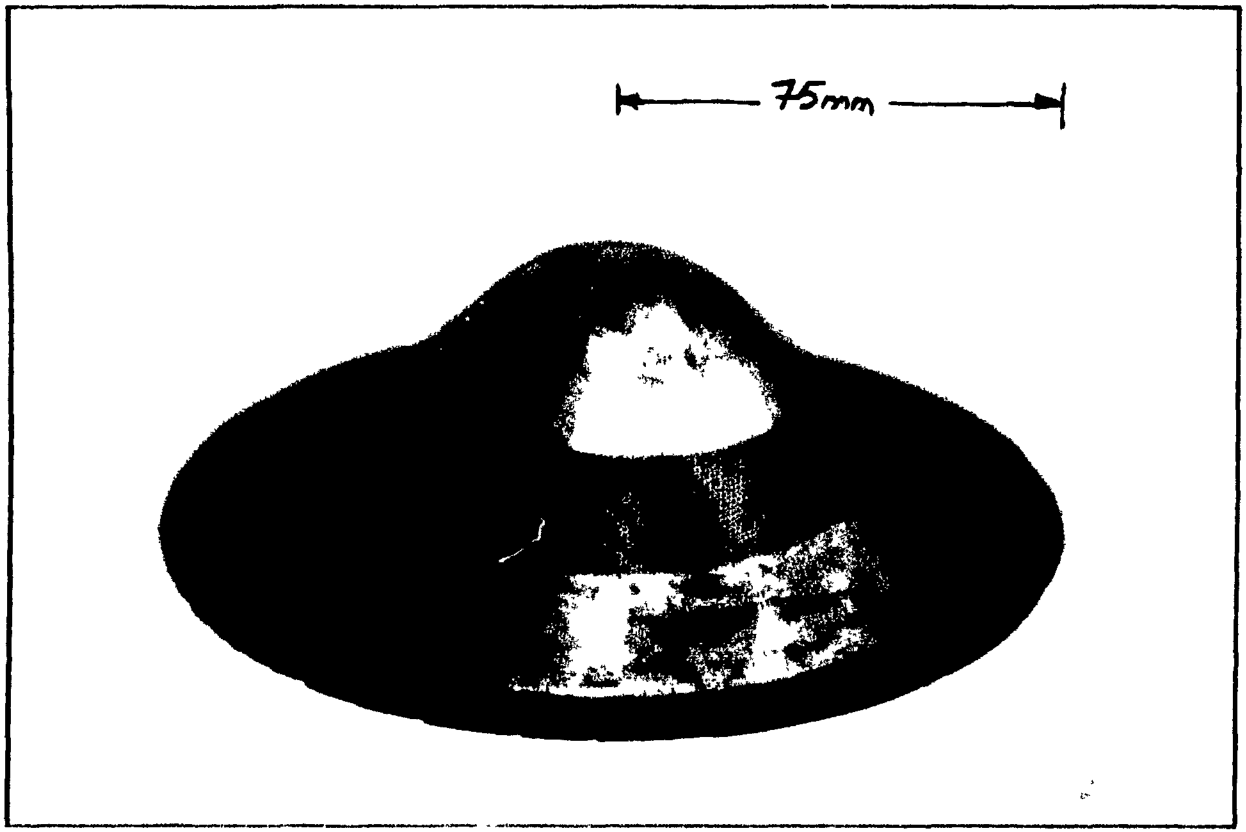

Figure 3.10 Photograph of the Focusing Lens

The lens (see Figure 3.10), was constructed from 5/1000" thick copper sheet. First, an aluminum mould consisting of both positive and negative segments was machined on a computerized lathe to the desired dimensions. The copper sheet was then sandwiched between an aluminum sheet, and the positive mould. The two sheets were then spun onto the mould to obtain the basic shape. It is difficult to spin thin sheets of copper without tearing the soft metal, and hence, the sheet of aluminum was necessary. Even with the extra sheet, the technicians could only obtain a success rate of about 1 in 3.

The successful cones were then annealed for 15 minutes at a temperature of 600°C. Annealing was necessary to soften the copper for the next stage in the shaping process. The annealing had to be performed in a furnace that was under vacuum to prevent oxidation of the copper surface. Though the oxide layer could easily be removed chemically, the process would make the lens too weak to retain its shape, and cause the thickness of the lens to be non-uniform. Attempts to prevent oxidation by providing a nitrogen flow through a furnace proved to be unsuccessful.

After annealing, the cones were pressed with a weight of 4000 pounds between the positive and negative moulds. This stiffened the cones into their exact shape. Wrinkles resulted in some of the cones during this compression stage as they required too much shaping.

The next stage in the process was to etch the grid pattern into the cones. This stage will be explained in detail since it is both crucial to the construction, and a somewhat unforgiving procedure.

Commercial photo-etching products from MG Chemicals[35], were used for the etching. The products consisted of #416 positive photoresist in aerosol form, #417 positive photoresist developer, and #418 positive photoresist etchant. (It is important to note that the photoresist aged, even in the aerosol form, and became ineffective for our purposes in about 2 months.)

The photoresist is a long chain polymer which breaks down when exposed to ultraviolet rays. The developer is an NaOH solution which will dissolve exposed photoresist, but has little effect on the long chain polymer form. The etchant is $FeCl_3$ which removes the exposed copper. The photoresist products are popularly used to create P.C. boards.

Other equipment used in the etching process included nitric acid for cleaning the copper, a 275 watt ultra violet lamp for exposing the resist, a turntable for rotating the cone during exposure, a small electric motor for spinning the cone to obtain an even coat of photoresist, an exposure mask and masking cone, cylindrically shaped tupperware dishes for bathing the cones in chemicals, and insulating varnish to protect the underside of the cone.

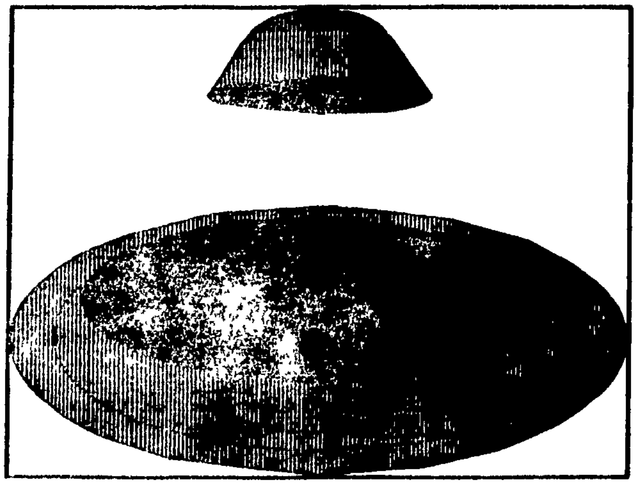
Figure 3.11 The Masking Cone

The electric motor for spinning the cone had attached to its shaft, a flat metal strip on which was glued an aluminum cone, shaped identically to the original lens. (A number of such cones were available as a byproduct of the spinning process).

The exposure mask used was a commercial graphics product which goes by the name Letratone (see Figure 3.12). A masking cone (see Figure 3.10) was fabricated from one of the byproduct cones. The strip removed from the cone had a width and location as determined previously for maximum performance of the spectrometer.

The following procedure was employed:

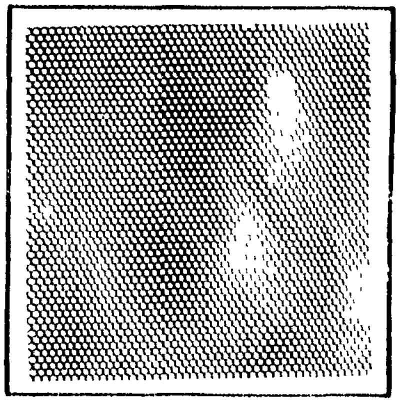

Figure 3.12 Exposure Mask: Letratone LT323

1. The underside of the cone was coated with a thin layer of G.E. Chemicals[36] insulating varnish and then dried.

2. The cone was cleaned in nitric acid of concentration 15%, and then quickly transferred to a water bath.

3. The cone was air dried, and placed in a fume hood on top of the mechanism designed for spinning it. A cardboard barrier was employed around the cone to capture splashes from the photoresist during spinning. Infra red lighting was engaged, as a thick layer of photoresist was sprayed on the cone. The cone was then spun quickly for 15 minutes to obtain a uniform coating of resist, before being placed in a dark environment to dry for 72 hours.

4. In a dimly lit room, the mask, cut to size, was positioned on the cone. Sizing and placement of the mask were not critical, as the mask was cut approximately 1 cm wider and 3 mm longer than needed. Once the mask was in position, excess length was trimmed, and a thin (1 mm) strip of scotch tape was attached to the underside of the overlapping region. This made the eventual removal of the mask much easier. Masking of the lens was completed by placing the masking cone over the lens. The hemispherical top of the masking cone was attached with a small quantity of double sided tape. The cone and its full mask were then centred on a turntable with the use of a plastic annulus which could be screwed down to the turntable.

5. The turntable was placed below a plate of 3/16" glass. The turntable was supported in an angular position such that the uppermost exposed area on the cone was horizontal. The 275 Watt ultra-violet bulb was situated 22" above this horizontal surface. The exposure time was 28 minutes. The rotation rate was one revolution per 50 seconds.

6. The mask was removed from the cone and it was placed in a bath of 4 parts water to one part developer solution. The container employed was gently shaken by hand. Development took approximately 3 minutes, but the ultimate criterion for determining sufficient development was the observation of a clear pattern. Increased lighting was necessary to make this observation. A good pattern had a dark orange colour for non-exposed portions, and copper showing in the exposed regions. Dark blue segments (not fully developed segments) were removed with cotton soaked in developer.

7. The lens was bathed in warm running water for 2 minutes.

8. The lens was placed in the etchant solution which was placed in a sink full of warm water. The solution was gently shaken by hand. Once some regions of the cone were completely etched through, caution was employed to ensure that the etching was relatively uniform. If it was found that some of the walls in the hexagonal pattern were deteriorating, the cone was rinsed in warm water, and individual regions of the cone were etched in an isolated fashion, using a wash bottle filled with the etchant solution.

9. Once a uniform pattern had been etched, the cone was placed in a running bath of warm water for 2 minutes.

10. The cone was placed in a solution of 1 part methanol, and 1 part toluene for approximately three hours. This removed both the photoresist, and the insulating varnish. The cone was then cleaned with isopropyl-alcohol.

3.5 Method Employed to Form Stainless Steel Mesh Cylinder

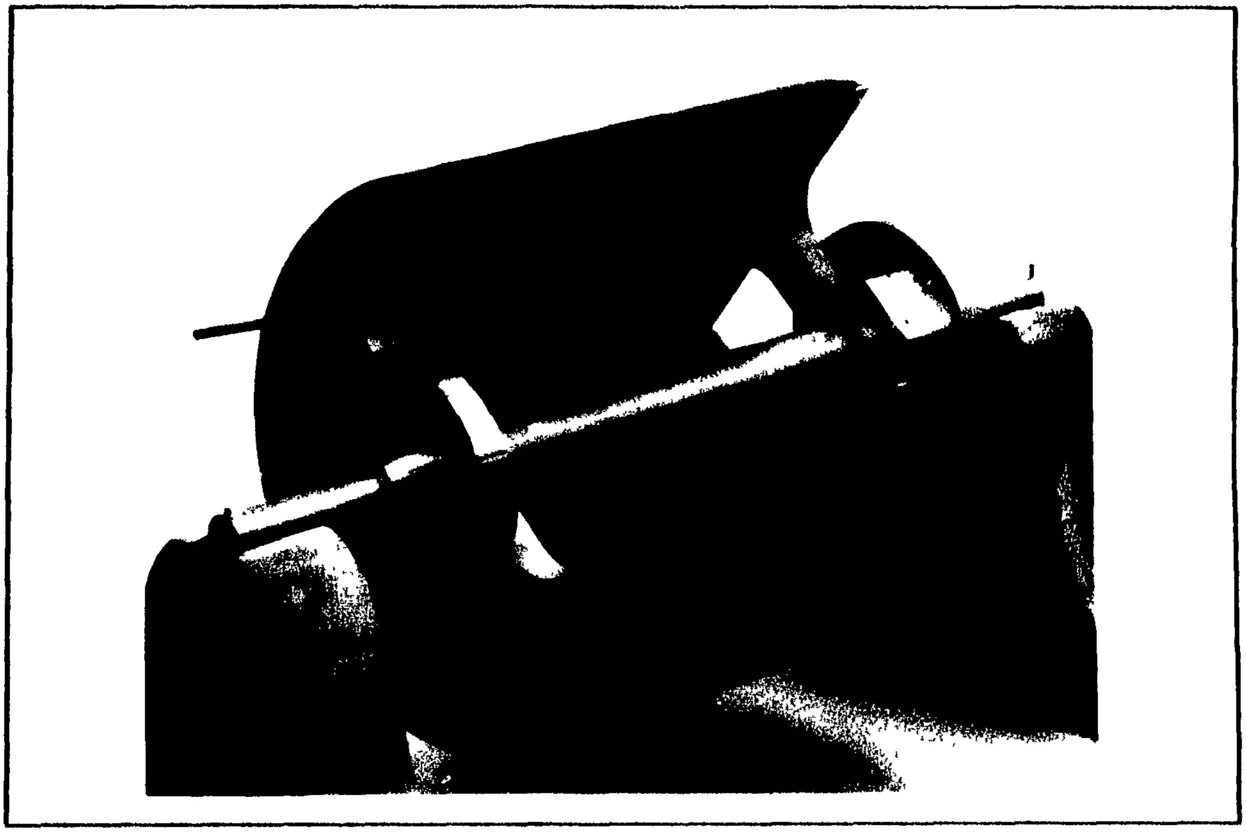

Figure 3.13 Photograph of the Mandrel

The stainless steel mesh used for most of the grids was not stiff enough to support its own weight. In order to form it into a 226 mm high and 200 mm diameter cylinder, support and tension were required. A collapsible mandrel (see Figure 3.13 and Figure 3.14), which the mesh could be wrapped around to form the cylinder, was thus built. The idea being that, after the mesh was glued to the ridges on the ring and bottom of the canister, the mandrel could be collapsed and removed.

The mandrel's cylinder was fabricated from a standard 8" PVC pipe, though it did have to be shaved down to the proper radius. The mandrel's ends were made of plastic, and the central rod with its accessories were aluminum. The procedure used to form the cylindrical grid was as follows:

1. The mandrel with its central rod and accessories was assembled.

2. The plate from the canister assembly was attached to the mandrel. One screw and one pin in each slice of the mandrel, held the plate in place.

3. The ring from the canister assembly, and the plexiglass plate from the foreplate assembly, was attached to the opposite end of the mandrel, in the same manner as in 2. (Note that the foreplate must be assembled after the canister assembly)

4. Three support rods, each 1 mm shorter than the rods that would eventually support the canister, were inserted through the holes on the outside of the plates, and ring.

5. A 1/1000" thick sheet of mylar was wrapped around the mandrel.

6. The mesh was cut to size allowing an inch of overlap where the seam would occur. The mesh was wrapped over the mylar such that the overlap at the seam was separated by the mylar.

7. While holding the mesh in place by hand, a wooden hoop, that could be tightened to the diameter of the mandrel was used to secure one end of the mesh.

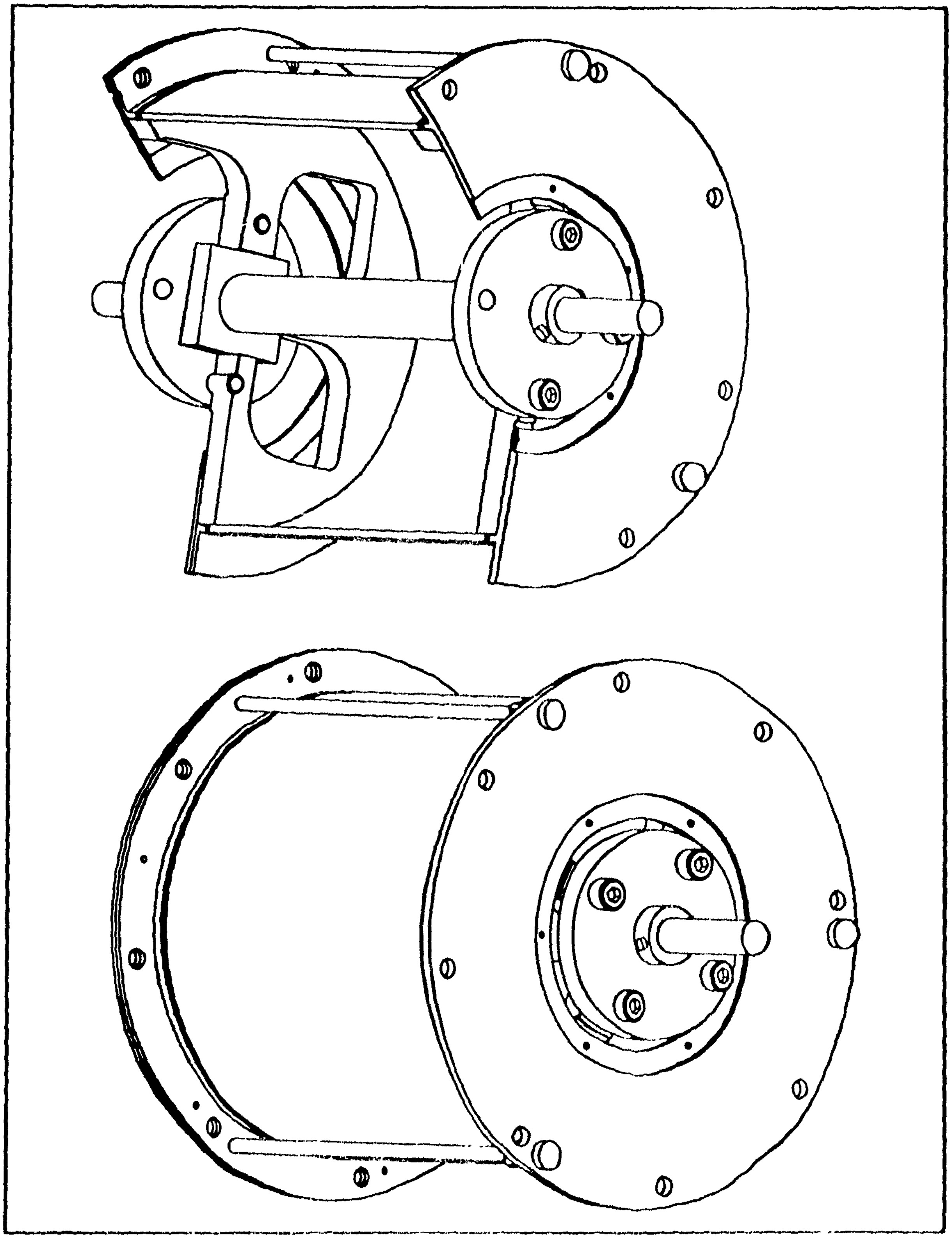

Figure 3.14 Fully Assembled Mandrel

8. A thick coat of Araldite glue was applied to the secured end of the mesh. A thick coat was needed to prevent electron discharges from the ends of wires.

9. After the glue cured, the other end of the mesh was glued in the same manner.

10. After curing, the support rods were removed.

11. The entire assembly was slid onto the three support rods that extend up from the chamber body. These rods were 1 mm longer than the former rods, so that when the nylon nuts at the top of the rods were tightened, the mesh was stretched 1 mm in the axial direction.

12. The plexiglass plate from the foreplate assembly was removed.

13. The mandrel was collapsed and removed, leaving the canister assembly.

14. Three coats of glue were applied along the seam to prevent electron discharges at high voltages.

3.6 Internal Wiring Connections

A thin high voltage, low current, miniature co-axial cable[37] was employed for the internal connections. Most of the wires were soft soldered to the commercial connectors in the bottom of the chamber, and attached with conductive epoxy at the other end. Ground connections were attached mechanically to screws in the bottom of the chamber. The curing stage for the conductive epoxy contacts was done under mylar so that smooth surfaces would be obtained. The mylar could be removed without disturbing the epoxy after curing was complete. A further layer of Araldite epoxy was then applied on top of the conductive epoxy to reduce electron discharges and add mechanical rigidity.

Chapter 4: Operation and Operating Characteristics of the Spectrometer

4.1 Control of Grid and Detector Potentials

Bertran model 602C power supplies were used to supply the potentials to the grids, and detector. 0 to -10 kV supplies were used for V1, and V2, and a 0 to -3 kV supply was used for the MCP detector.

The output voltages were controlled by remote inputs. A 0 to +5 V dc analog input signal being proportional to the maximum rated output voltage. A fixed 5 V supply was available from each of the power supplies, and these supplies were used with standard 10 turn potentiometers, equipped with counting dials, to control the input voltages. Since the resolution of the spectrometer was established by the ratio V2/V1, the wiper from the V1 potentiometer was used to supply the upper voltage for the V2 potentiometer as in Figure 4.1. The resistance of the V1 potentiometer needed to be much smaller than that for V2, so that the parallel resistance seen by the wiper from the V1 potentiometer will not be significantly different from its corresponding value if the V2 potentiometer were removed.

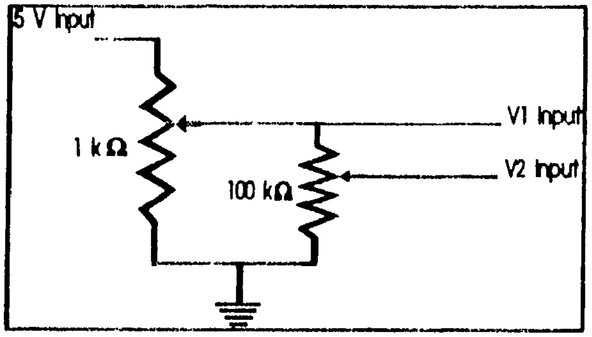

Figure 4.1 Wiring Schematic for Keeping V2/V1 Constant

The control panel also had a BNC connector for external input voltage to allow V1 to be swept at fixed V2/V1, and hence, fixed resolution. Further BNC connectors allowed us to monitor the output voltages of each supply. (The supplies were equipped with both kV and mA monitor terminals.)

The power supplies produced a .0005% 20,000 kHz ripple. It was found that the ripple coupled strongly with the voltages on the grids and the collector anode, making it impossible to observe the electron pulses. RC filters were therefore inserted on the lines from the power supplies to their respective components. One megaohm resistors with .01 μF ceramic capacitors were found to provide a long enough time constant to effectively eliminate the ripple coupling. The filters were housed in a plexiglass box since high voltages would otherwise be exposed.

4.2 Safety Features of the Apparatus

A number of safety features needed to be added to the system to prevent damage from occurring in the event of a power or water cut.

The first was a standard thermal switch on the diffusion pump. If the cooling system failed, and the diffusion pump overheated, power was cut to the heater.

The second was a pushbutton relay system (see Figure 4.2 a)) that kept the diffusion pump from being restarted after a power cut. This allows the operator to check that the diffusion pump is operating in a vacuum environment before it resumes pumping. Lighted pushbutton switches were used to turn the pump on and off.

The third was a pneumatic valve control system that sealed off the vacuum chamber in the event of a power cut. This was necessary to prevent the possibility of oil being drawn into the chamber. In the event of a power failure, a solenoid valve, which controlled air pressure to the pneumatic valve, would close, causing the chamber valve to also close. A relay system (see Figure 4.2 b)) prevented the valve from being reopened until the operator made this choice.

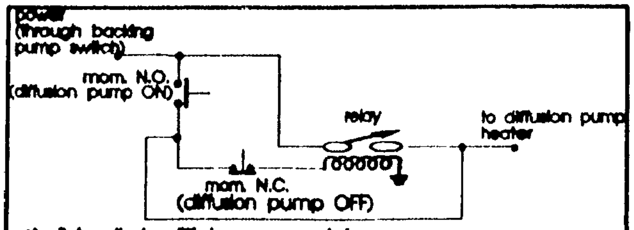

a) Schmatic for diffusion pump control.

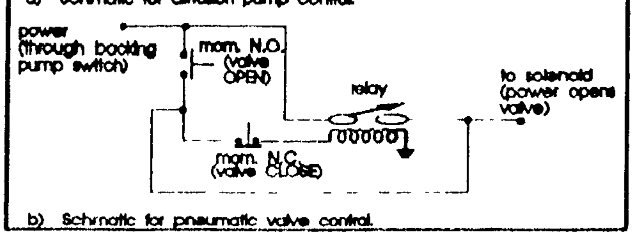

b) Schrnatic for pneumatic valve control.

Figure 4.2 Schematics for Diffusion Pump Control, and Pneumatic Valve Control

Lighted pushbuttons controlled the opening and closing of the valve under normal operation. Micro-switches in the top of the diffusion pump, that switch depending upon the condition of the valve, controlled the lights for the pushbuttons so that the operator could always check the state of the valve.

The fourth, and most important safety feature, acted to cut power to the grids and detector in the event that a) the pressure in the chamber rises above 4×10^{-6} torr, or b) a current surge is produced in one of the power supplies. This action is necessary since the detector will be damaged if it operates in higher pressures, or it could be damaged if electrical arcing occurs within the chamber. Power can not be reinstated to the supplies until the currents and pressure are within safe limits, and the operator has pushed a button to resume operation.

There are nine indicator LEDs which define the state of the system. Four red LEDs illuminate to indicate which, if any, of the elements are currently not within safe limits. Four green LEDs indicate, if they are not illuminated, that the corresponding element has malfunctioned. A ninth green LED can only be illuminated through the positive action of pressing a pushbutton while all the elements are within safe limits (no red lights on), and it signifies that power is available for the supplies.

In normal operation, a red light would be on while the chamber pumps down. Once the pressure is low enough, the red light would go off, and the operator could then push a button causing all 5 green lights to illuminate, signifying that the grids and detector could now be powered. If now for example, an arc were to occur from the main cylindrical grid, the corresponding red LED would light momentarily. The corresponding green LED goes out, and stays non-illuminated until the pushbutton is used again. In this way, the operator not only knows if an element is not within safe limits, but also which element triggered a shutdown.

Two methods were used to shut down the power supplies. The first, and most reliable, was with a relay switch. When an element triggers a shutdown, the relay switch opens the a.c. line into the supplies. The switch can not close again until the problem has been fixed, and a pushbutton has been depressed. The second, faster method of shut-down, was to use a transistor to sink a tripping terminal available on the supplies. This method is not as reliable since the transistor could fail to sink the terminal, but it was much faster so that the immediate shutdown is achieved using the transistor circuit, and the permanent disabling of the power supplies follows when the relay is opened.

The pressure gauge had a voltage recorder socket available, which produced a 0 - 10 volt potential, proportional to the logarithm of the pressure reading, and the power supplies had a current monitor terminal which produced a voltage of 0 - 5 volts, proportional to the maximum output current of the supplies (1 mA for the 10 kV supplies, and .5 mA for the 3 kV supply). These four lines provided all the necessary information for tripping the power supplies.

The electronic circuitry employed to trip the supplies is shown schematically for a single element in Figure 4.3. Elements in the figure above the dotted line are replicated 3 more times corresponding to the other three triggering criteria. Standard operational amplifiers, in an adjustable Schmitt trigger configuration, were used to establish triggering points and hysteresis. The opto-couplers were used to interface with TTL logic. That is, the 0\15 volt signal from the Schmitt trigger induce a 5\0 volt signal at the collector of the of the opto-coupler, which could then be used to trigger the binary states of TTL. The flip flops kept track of the state of the system. The inverters leading to the power supplies have open collector outputs. That is, they have an external pull-up resistor on their output, and as such act to buffer the high voltage states that keep the power supplies enabled.

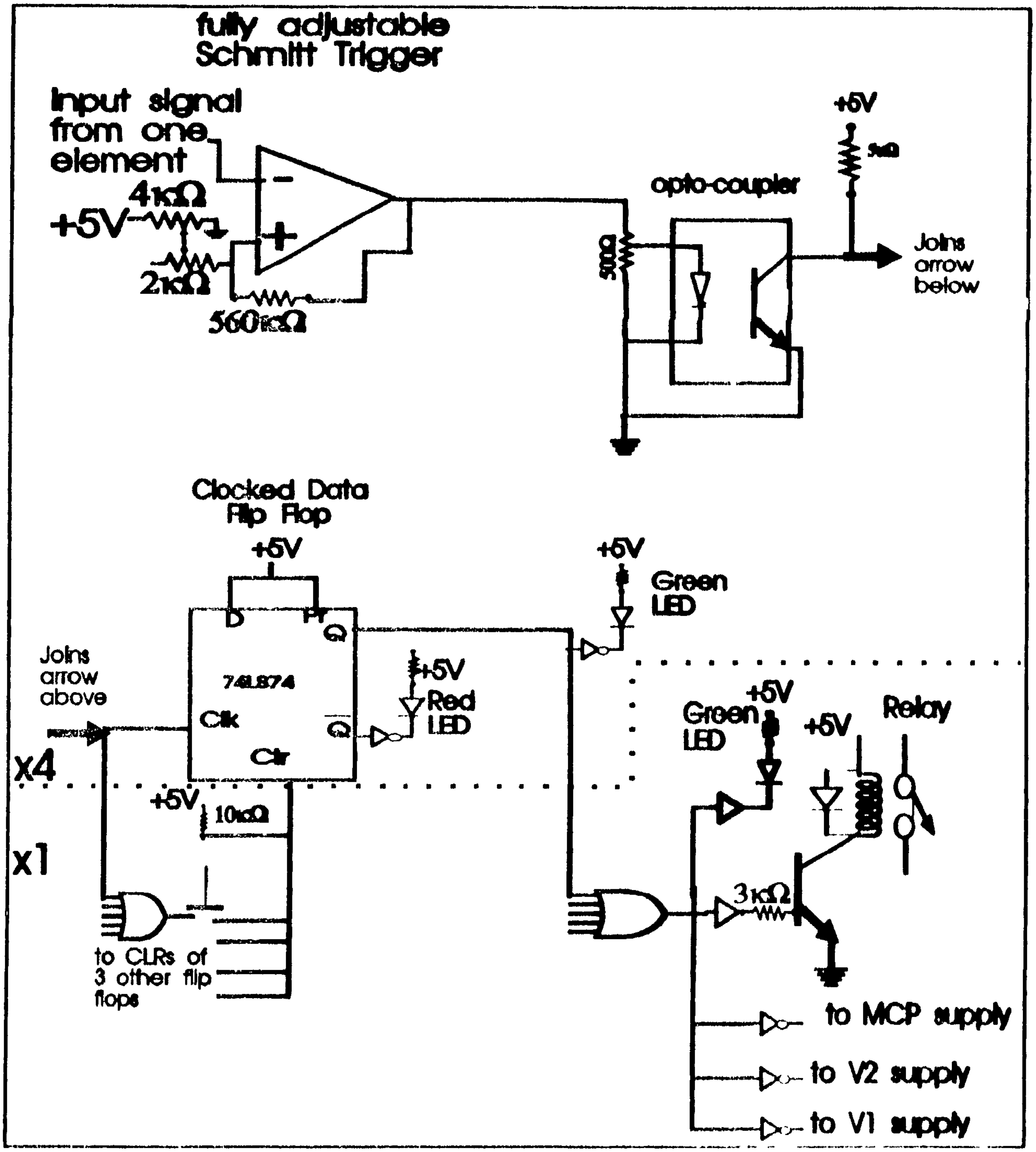

Figure 4.3 Schematics for Grid and Detector Automatic Shutdown Feature

4.3 Vacuum Characteristics

An Edward's "Diffstak Mk2 100" diffusion pump with a rated pumping capacity of 280 litres/s was used to pump down the 20 litre chamber. An ultimate pressure of $1x10^{-7}$ torr was obtained with no internal parts enclosed in approximately 45 minutes. With internal parts, an ultimate pressure of $2x10^{-7}$ torr was eventually reached after ~3 months of pumping .

Most of the outgassing of the system can be attributed to the plexiglass surfaces. Plexiglass is somewhat hygroscopic, and a bake-out was required to remove the surface water molecules. A heating cable, wrapped around the chamber, was used to obtain a temperature of 65°C on the surface. Tests demonstrated that temperatures greater than 80°C would deform plexiglass on the inside of the chamber. At a temperature of 65°C, a bake-out of 24 hours was required to reach a pressure of $2x10^{-6}$ torr, which is the highest pressure at which the detector may be operated without ion feedback. The ultimate pressure of $2x10^{-7}$ torr was reached ~3 months after this time. The internal components were either in an argon environment, or in vacuum for this 3 month period. The outgassing rate of the plexiglass, after such a long period, is believed to be lower than that found in the literature since the ultimate pressure that we reached was lower than that calculated, based on the outgassing rate given in the literature. Plexiglass has an outgassing rate of $9.77x10^{-7}$ $torr \cdot l \cdot s^{-1} \cdot cm^{-2}$ [38], and given the pumping speed, volume, and the area of the exposed plexiglass(~1000 cm^2), an ultimate pressure of $4x10^{-7}$ torr should have been reached.

4.4 Sample Changing

The long bake-out time, together with fact that the MCP should not be exposed to air at atmospheric pressure, made it necessary to create a gas line and valve leading into the chamber, so that samples could be changed readily.

To change samples, the following procedure is followed.

1. The voltage to the grids is cut.
2. The top valve on the diffusion pump is closed.
3. The chamber is filled with argon to atmospheric pressure.
4. The top flange with the sample is removed, and replaced with blank flange, and the sample mount is removed from the original flange.
5. Another sample mount with the new sample is screwed into the flange, and then it replaces the temporary flange presently on the top of the chamber.
6. The chamber is pumped-down.

(It takes approximately one hour for the chamber to be pumped down to working pressure.)

4.5 The Detector and Data Acquisition Systems

The detector was made by Galileo Industries[39]. It consisted of two matched MCPs (usually referred to as a chevron). Physically, an MCP is a thin glass wafer with an array of approximately 10 μm diameter holes through it, and each hole acts as a miniature channel electron multiplier [CEM]. A CEM is special formulation glass tube which is heavily doped with lead. This special material has a combination of high resistance (~10^8 Ω), and a high secondary emission coefficient. In a vacuum of better than 10^{-6} torr, a potential of a few thousand volts is applied across the CEM, and when an incident particle or photon of sufficient energy strikes the inside surface of the channel, at least one secondary electron is emitted. The incident particle must strike the wall of the channel at an angle such that sufficient energy is imparted on the surface for photoemission. The secondary electron(s) is then accelerated by the electrostatic field until it hits the interior surface of the channel. If the electron has accumulated enough energy, more than one secondary will be released. This process will occur 10 - 20 more times in a CEM, resulting in a gain of the order 10^3. The gain is dependent upon the ratio of the length to the diameter of the channel.

If the gain reaches $\sim 10^4$ a condition known as ion feedback occurs. The density of electrons at the exit end of the channel becomes so great that residual gas molecules in the channel are ionized. These ions are then accelerated towards the input end causing electron emissions. The emissions due to the ions result in spurious pulses at the output not representative of the input. CEM's are often curved to reduce ion feedback. The curvature reduces the distance that the ion can travel in the channel, and since, the output pulse is proportional to the distance over which the secondary electrons can cascade towards the output, the ion produced pulses are much smaller than the signal pulses.

The fact that the gain of the CEM is dependent not on the length or diameter of the channel alone, but rather on their ratio, makes possible the idea of miniature channels with high gain characteristics. As was mentioned, MCP's are arrays of thousands of miniature CEM's connected in parallel. A thin metal electrode (inconel or nichrome) is vacuum deposited on both input and output surfaces of the plate to electrically connect all the channels in parallel. A chevron is a set of two MCP's which are sandwiched together. The holes in the plates are bored at an angle of 8° to the face of the plate, and so when the plates are set against each other, the holes meet at an angle. This has the same effect as curving the channel of the CEM. That is, ion feedback is reduced, and high gains ($\sim 10^6$) may be achieved.

MCPs are usually used either in applications where imaging is required, or such as in our case, where the required detector area is large.

The characteristics of our detector (Galileo model 3040) were as follows:

- 40 mm active diameter
- 25 μm hole size
- 32 μm centre to centre spacing
- .5 mm thickness per plate
- gain between 10^5 and 10^7 (see Figure 4.4)
- operating pressure $< 2\times10^{-6}$ torr (see Figure 4.4)
- electron detection efficiency (see Figure 4.5)
- dark count rate - 4-10 counts/s

The typical potential configuration about our detector is shown in Figure 4.6. Electrons that pass through the grid in the back plate, are accelerated through more than 5000 volts to the detector. The burst of electrons at the output of the detector is then accelerated towards the anode through 300 volts. The

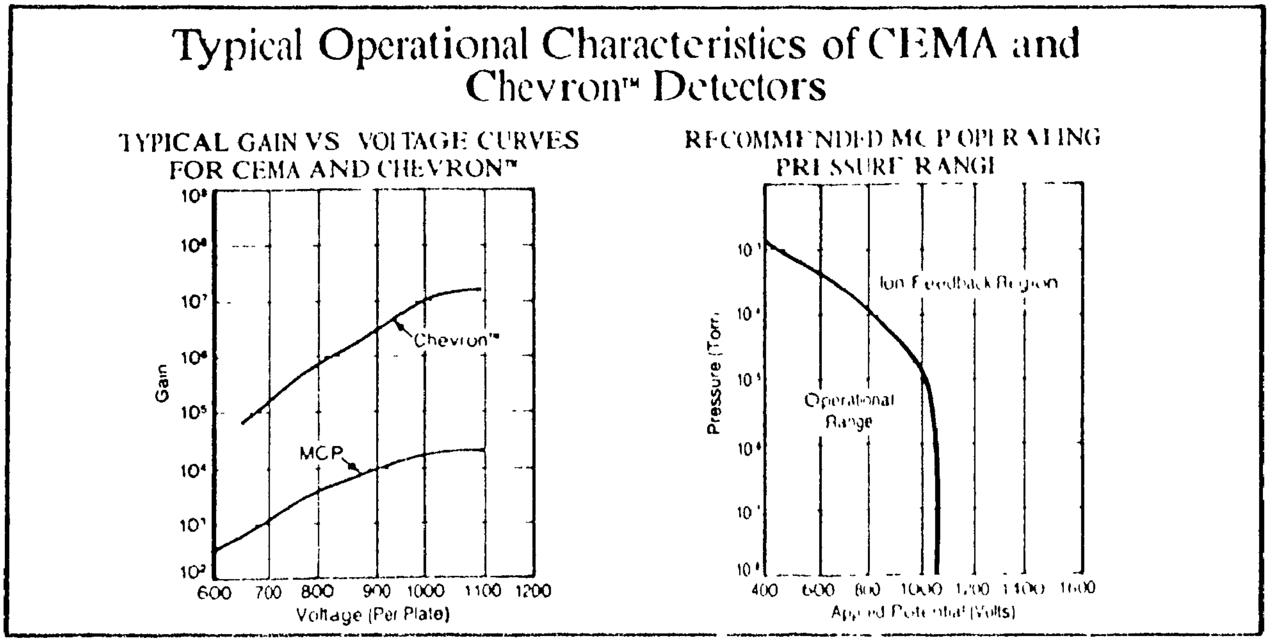

Figure 4.4 Gain and Pressure Characteristics of the MCP Detector

spectrometer can not detect electrons with pass energy below about 1500 eV, since the canister will be at a potential that is positive relative to the detector. That is, the canister must be set to a voltage of nearly -1500 volts in order to select 1500 eV electrons, and the front of the detector must be set to approximately -1500 volts to operate, so there will be no potential to accelerate the electrons into the detector, and therefore, pass energies below 1500 volts are not selectable. Ideally, the detector and anode collector should be at potentials

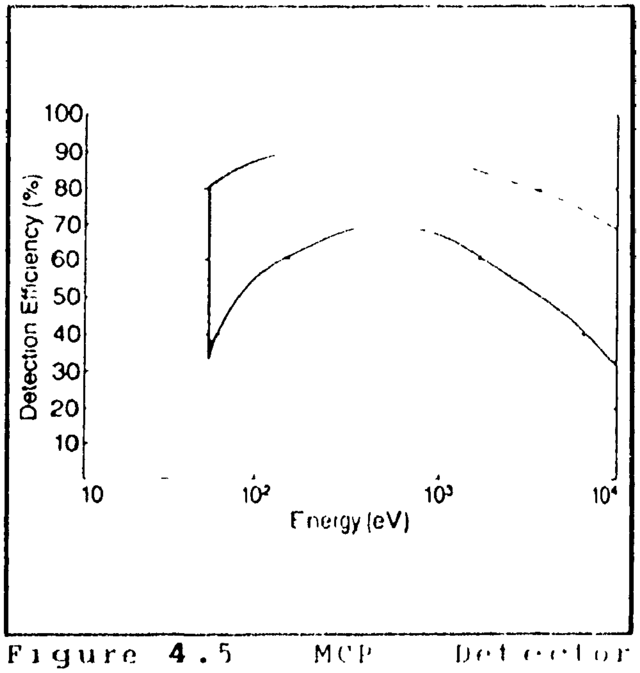

Figure 4.5 MCP Detector Efficiency Characteristics

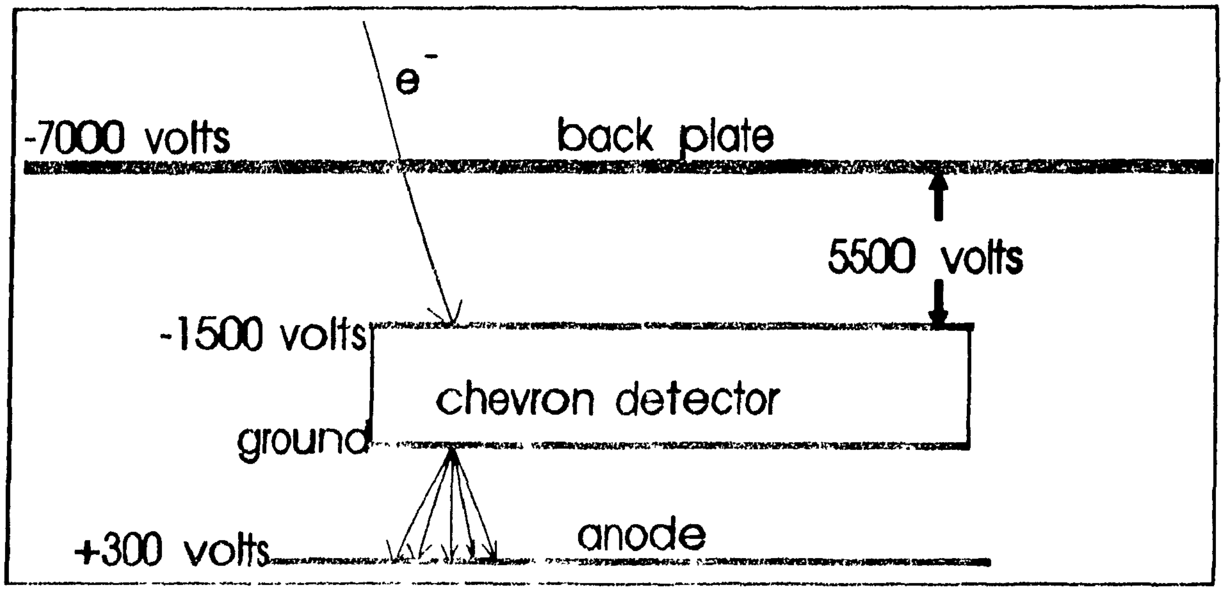

Figure 4.6 Typical Potential Configuration About Detector

that are fixed with respect to the canister voltage, as in Figure 4.7, so that the electrons enter the detector at energies (~300eV) corresponding to maximum detector efficiency, and so that lower pass energies may be detected.

The data acquisition system was composed of the following commercial products:

- preamplifier, Canberra model 102E
- amplifier TSCA, Canberra model 2015A
- velocity transducer, Wissel model MR360
- function generator, Wissel model DFG1000
- ratemeter, Canberra model 2081

The multichannel analyzer was supplied by EG&G Ortec. It consisted of a software package and card, and was designed for a standard personal computer.

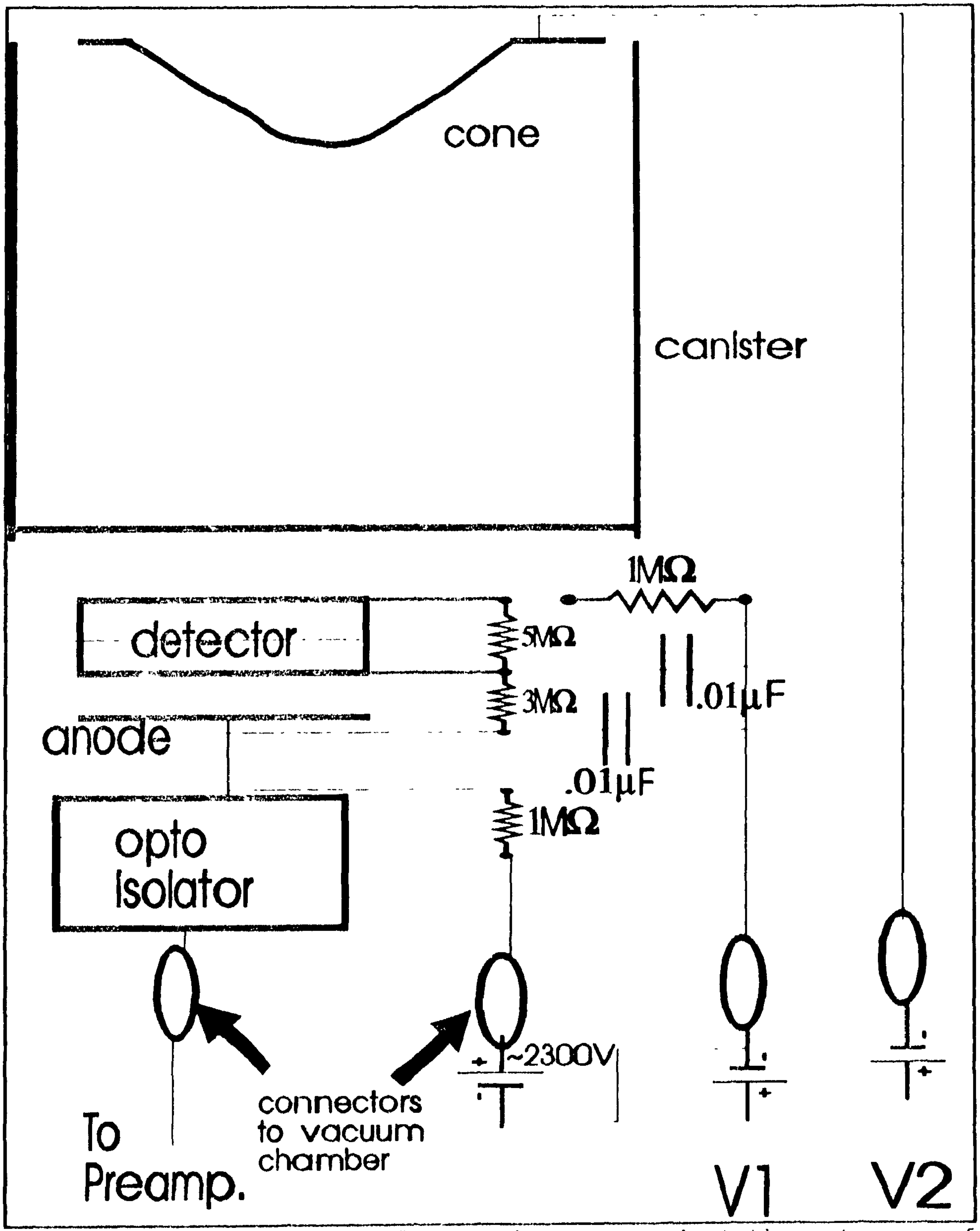

Figure 4.7 Schematic for fixing the potential at the entrance of the MCP with reference to the canister voltage, V1.

Chapter 5: Observations and Characteristics of Spectrometer Performance

5.1 Background Characteristics

The MCP detector produced a background count rate of between 4 and 10 counts per second, depending on the voltage applied across the plates (1400 to 1900 volts). Lower voltages produced smaller background, but were more prone to intermittent noise bursts. The cause of these bursts has not yet been ascertained, but is believed to be a grounding or electrical contact problem. The effects of the disturbances was mitigated by operating the detector at a high gain potential, which produced typical pilses that were 10 times as large as the noise bursts. The smaller noise bursts could then by filtered-out by the pass window of the SCA. The result was a background count rate of 9±1 counts/s.

The effect of applying a potential to the grids, produced a secondary background. There are two possible causes of this background. One possibility is that electrons are being emitted from the conductive epoxy contacts, and the other possibility is that the surface roughness of the grids themselves is producing electron emissions. In either case, some of the emitted electrons would strike the detector directly, and others through collisions, would cause ions to be freed. The ions have a greater probability than the electrons of being pulled into the detector due to the negative potential along the backplate of the spectrometer, and hence, a considerable background would develop as the potential on the grids increases.

It was found that the amount of this type of background alone, for a potential V1, rose from 8±1 counts/s at V1 2000 volts to 42±2 counts/s at V1=8300 volts, in a roughly linear manner. In addition to this, the background due to the grid at V2 introduced 20±2 counts/s at V1=8300 volts and V2/V1=.5. For a typical ^{57}Fe Mossbauer spectrum where V1 would be set to approximately 6800 volts, and for resolutions of 4.3%, 3%, and 2.1% respectively, the backgrounds from the grids were 24±2, 29±2, and 37±2 counts/s.

Another source of background was from photoelectrons and γ rays, introduced by the activity of the source. The action of bringing the source from a position where it could not interact with the detector, to its mounted position 75 mm from the sample (90% enriched 8x10 mm 310 stainless steel), increased the count rate by 8±2 counts per second with a closed aperture, and by 26±2 counts/s with the aperture open. These measurements were performed with the potential V1 set at 6800 volts and V2/V1 0, which corresponds to a pass energy equal to the K conversion electron energy 7300 eV, and minimum resolution, 4.3%. 8±2 counts/s of background must therefore be attributed to γ-rays directly striking the detector, and 18±3 (26±2 - 8±2) must be attributed to photoelectron effects created by the γ-rays.

5.2 The Energy Spectrum of Emitted Conversion Electrons From ^{57}Co

The first sample to be used in the spectrometer was a thin film of radioactive ^{57}CoCl$_2$ [40]. Preparation of the sample was accomplished by allowing a droplet of a dilute solution of ^{57}CoCl$_2$

in water to evaporate on aluminum foil. The sample was approximately 8 mm in diameter, and had an activity of ~$1x10^6$ Bq. The activity was determined by comparing the count rate from a sample of known activity to that of the used sample. There were several reasons for this choice of sample. Firstly, it eliminated the need for an external source. Secondly, it produced of the order, 10^2 as many K conversion electrons/s as would be expected from an enriched Fe sample bombarded by γ-rays, and hence, counting times would be comparatively short. Thirdly, the ^{57}Co sample provided an opportunity to test the spectrometer's ability to select a pass energy and a resolution. This is because there are three dominant conversion electron processes that produce mono-energetic electrons. These include, K conversion processes which produce 7300 eV electrons, KLL conversion processes which produce 5600 eV electrons, and KLM processes which produce 6500 eV electrons. The count rate peaks produced corresponding to these conversion electrons would allow us to see if the spectrometer can select a pass energy, and to compare the resolution of the spectrometer to that predicted by the computer simulations.

The last reason for choosing the ^{57}Co sample was that the resultant emission spectra has been a standard test for previously constructed DSCEMS spectrometers, and as such it provides a direct comparison of our spectrometer to others like it. In particular, it will allow us to compare our count rates to that of the original spectrometer.

The electron emission spectra for ^{57}Co were obtained by supplying a discretely and linearly, increasing input voltage, into the supplies, which produced a proportional output voltage at the grids. The 500 channels of the multichannel analyzer advanced every 10 seconds in synchronization with the discrete jumps in the input voltage. Only one sweep through the 500 channels was made. Each channel represented an advancement of 16.7 volts to the potential V1, so that the maximum applied voltage to the 'canister' was 8300 volts.

Figure 5.1 shows the electron emission spectra for predicted resolutions of 2.1%, 3%, and 4.3%. The vertical scale is in counts/s, and the horizontal scale is the number of volts applied to the 'canister'. The data will be discussed in the section 6.2.

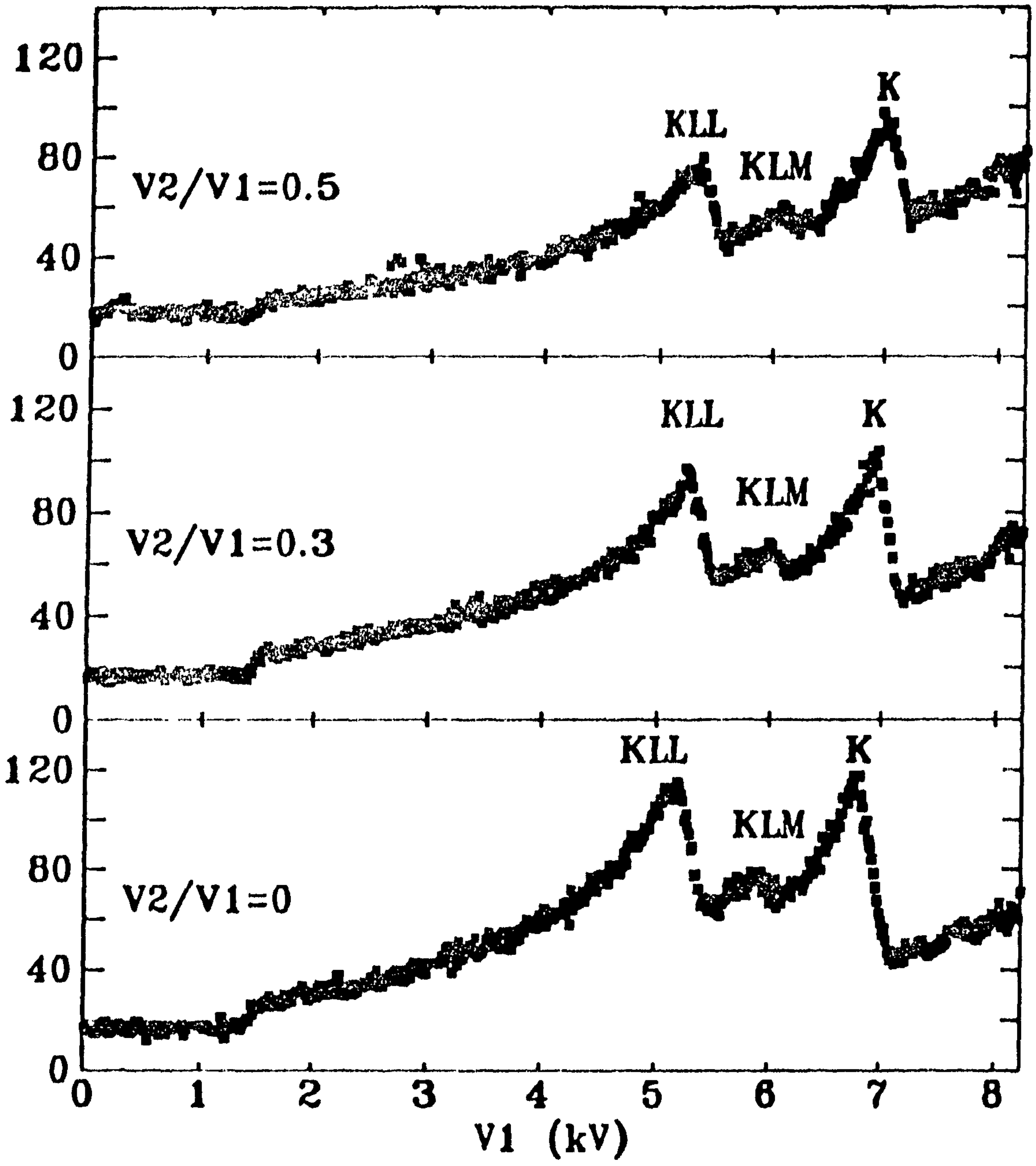

Figure 5.1 Conversion Electron Spectrum from ^{57}Co for Resolution Settings of 2.1% (top), 3% (middle), and 4.3% (bottom)

5.3 Attempt to obtain a Mossbauer Spectra from an Enriched Stainless Steel Sample

A layer of 90% enriched 310 stainless steel (8x10x.0013 mm^3)[41] on an aluminum substrate was used to obtain a Mossbauer spectrum. Stainless steel was employed since its spectrum contains a strong single line with a very small isomer shift relative to ^{57}Co. The strong single line feature reduces counting times, and the fact that there is a very small isomer shift, facilitated the ability to obtain resonance by turning off the velocity transducer. If the signal is strong enough, a count rate increase should be readily visible on a rate meter when the drive is turned-off and resonance is obtained.

The activity of the source used was 24 mCi, and it was located 75 mm from the sample. A lead aperture, located 35 mm from the sample with an opening of diameter 5 mm, was used to reduce the diameter of the outcoming beam so that it would pass cleanly through the 20 mm diameter bore in the sample mount.

Turning the velocity transducer on and off produced no noticeable increase in the count rate. A signal rate of 2 counts/s would have been observable on the rate meter, and hence, the signal must have been less that 2 counts/s. Since the total background count rate was 59±3 counts/s, long counting times could be assumed.

There was no sign of the peak, even after 71 hours of counting. During this time approximately 30,000 counts were obtained per channel. There were 512 channels. A background count rate of as small as .7 counts/s would have produced a signal equal to twice the noise in the background in this amount of time, and therefore the signal rate must have been less than .7 counts/s. An analysis of the reasons for the failure to produce a peak will be given in section 6.3.

Chapter 6: Evaluation of Spectrometer Performance

6.1 Comparison of Experimental Pass Energy and Resolution Settings to that Predicted by Computer Simulations

The location (V1 setting) and resolution of the K peaks were compared between the computer simulated results and the experimental results. The simulated V1 settings were calculated by assuming a beam of monoenergetic 7300 eV electrons, and then employing the values in Table 2.2. The resolution of the experimental peaks was calculated as twice the width of the high energy (hard) side of the peak at half maximum. The low energy (soft) side of the peak is broadened due to energy losses created as electrons travel towards the surface. It should be noted that the contribution of 14.4 keV M conversion electrons to the broadening of the hard side of the K peak, should not be significant since the number of M conversion electrons much smaller than the number of K conversion electrons (~1/7), and more importantly, the energy of the M conversion electrons is double that of the K conversion electrons. It is therefore very unlikely that an M conversion electrons which will lose just enough energy to lie on the hard side of the K peak.

Table 6.1 Comparison of Location and Resolution of K Peak between Computer Simulations and Experiment

	Simulated		Experimental	
V2/V1	Resolution	Peak Location V1 (volts)	Resolution	Peak Location V1 (volts)
0	4.3%	6862	4.26±.24%	6850±17
.3	3.0%	7008	2.98±.36%	7000±17
.5	2.1%	7118	2.45±.46%	7130±17

The resolution and potential settings agree within the experimental uncertainties of those predicted by the computer simulations.

In Table 6.2, the position of the KLL peaks in Figure 5.1 was compared with the computer simulation predictions to see if the spectrometer worked as predicted for pass energies other than 7300 eV. The simulated predictions for the locations were obtained by assuming a beam of monoenergetic electrons of energy 5600 eV, and then using the values given in Table 2.2.

Table 6.2 Comparison of Location of KLL Peaks between Computer Simulation and Experiment

	Simulated	Experimental
V2/V1	Location of Peak V1 (volts)	Location of Peak V1 (volts)
0	5264	5326±17
.3	5376	5432±17
.5	5460	5511±34

There is a consistent upward shift of about 50 volts (~1%) in the locations of the experimental peaks as compared to the predicted values. The value of 5600 eV for the KLL conversion energy was known to only two decimal place accuracy, and the upward shift may be a reflection of the next decimal place.

6.2 Comparison of Count Rate with the Prototype's, Based on Conversion Electron Spectrum of ^{57}Co

The K conversion peak of the electron spectrum from ^{57}Co for the spectrometer by van Noort, and van Gorkum, produced approximately the same amount of signal as ours. We had a count rate of 120±3 s^{-1} at the K peak (broadest resolution), and they had a count rate of ~116 s^{-1}. Our sample was 10 times as active, and hence, it might be expected that our signal would be 10 times as large. Two factors account for the fact that this was not the case. The first is that our sample was thicker, and the second is that our spectrometer performance was not as high.

A thicker sample will have a higher photon count rate, and therefore higher apparent activity, but will not have a proportionally higher electron count rate, since the electrons will be absorbed during their travel to the sample surface. All electrons that are the products of nuclear events that occur at depths greater than about 300 nm will not escape from the sample surface. The most telling evidence that our sample was thicker than that used by van Noort et al. is that our KLL conversion peak is considerably broadened on the soft side (lower pass energy). The half width (soft side) at half maximum is 10% of the pass energy for their peak, but 14% for our peak. The difference is due to K conversion electrons which were able to escape from our sample, but originated from depths that were greater than the thickness of their sample. If for instance, our sample is 600 nm thick, fully half or our activity will not result in signal due to electron absorption. Since the only difference in the spectrum created by sample thickness was a slight broadening of the peaks, efforts were not made to prepare a thinner sample.

Some of the detection and transmission properties of our spectrometer were lower than that of their spectrometer, and this accounts for the remainder of the difference in the intensity of the K peaks. For instance, the prototype spectrometer employed an extended channeltron type detector that was at a potential which was fixed with respect to the potential of the backplate. Incoming electrons were accelerated to an energy that maximized the efficiency of the detector. Such a detection system should detect 85% of the electrons the incident electrons[42]. The K conversion electrons should reach the front of our MCP detector with an energy of about 5500 eV (see Figure 4.6). The detection efficiency of the MCP is rated between 40% and 70% for electrons of this energy (see Figure 4.5). We therefore expect a drop in our count rate of between 1.2 and 2.1.

Our transmission was also slightly lower than that of the prototype. This was primarily due to the fact that our grids were less transparent, but also because our acceptance angle was slightly smaller. The entrance grid and detector grids of their spectrometer had 93% transmission, whereas ours had 90% transmission. Their cone had 81% transmission, and our cone had 55% transmission. Their total grid transmission was therefore .70

(.93x.93x.81) and our grid transmission was .45 (.90x.90x.55). The difference in the transmissions accounts for a factor of 1.55 in the count rates. Our acceptance angle was slightly smaller than that of the prototype's. This is best reflected in the fact that our widest resolution was 4.3%, whereas their widest resolution was 5%. We therefore expect a variation in the count rate owing to the difference in the acceptance angles of approximately 1.16 (5%/4.3%).

Spectrometer performance therefore accounts for a factor of between 2.16 (1.2x1.55x1.16) and 3.78 (2.1x1.55x1.16) in the drop in count rate (factor of ~10) between our spectrometer and that of van Noort et al. The remaining drop in count rate must be due to sample thickness. Our sample must have been approximately 3 times as thick as that of used by van Noort et al. to account for the difference in count rates.

6.3 Theoretical Signal for Stainless Steel Mossbauer Spectrum

The following is a calculation of the expected signal rate from the Stainless Steel sample:

Photons from 24 mCi source (26 mCi source after 31 days with 270 day ½ life)	... $8.9\times10^{8}\ s^{-1}\pm2\%$
Fraction that will hit 8x10 mm sample 75 mm away. (Assume imperfect alignment and middle aperture result in an effective diameter of 8 mm.)	... 1/1400±5%
Photons striking sample	... $6.4\times10^{5}\ s^{-1}\pm5.3\%$
Fraction which will result in a conversion electron[43]	... 1/100±10%
Conversion electrons from sample	... $6.4\times10^{3}\ s^{-1}\pm11\%$
Fraction of conversion electrons which are K conversion electrons falling within the	

passband (see explanation below)	... 1/100±30%
K conversion electrons from sample within pass band	... 64 s^{-1}±23%
Fraction lost due to the transmission and detection properties of the spectrometer	
Acceptance angle (5% of 4π)	... 5/100±5%
Grid Transmissions (90%,55%,90%)	... 45/100±3%
Efficiency of detector (see Figure 4.5)	... 50/100±20%
Striking fraction (see section 2.3c))	... 60/100±10%

* * *

Predicted Signal Rate ... 0.4 s^{-1}±40%

* * *

The estimation for the fraction of conversion electrons that would emerge from the sample within the pass band of the spectrometer is based on the following data. About 10% of all conversion electrons are K conversion electrons. The average energy of a conversion electron is ~5000 eV, and hence, it can be estimated that it is roughly 1.5 times (7300eV/5000eV) more likely that a typical conversion electron will be absorbed in the sample than it is for a K conversion electron. 15% (10%x1.5) of conversion electrons emerging from the surface will therefore be K conversion electrons. The fraction of the K conversion electrons that will fall in the pass band can be estimated in the following manner. The stopping power exerted on a electron in Fe is ~1.4 eV/Å[44]. The passband is 4.3% of ~7000 volts, or within ~300 volts of the pass energy. This corresponds to an escape depth of range ~200A. K conversion electrons have an escape depth of ~3000Å (note that it is not correct to use the stopping power directly in this case because of angular effects, and so the often quoted escape depth range of conversion electrons is employed), and therefore, roughly 7% of the K conversion electrons will fall within the pass band. The fraction of conversion electrons falling within the passband is therefore ~1/100 (15%x7%).

Our predicted signal count of .4 counts/s would result in a peak height equal to twice the random noise in the background (59±3 counts/s), in approximately 210 hours of counting time. That is, the peak should become observable after less than nine days of collecting data.

The similar transmission characteristics of the CMA spectrometer constructed by Sauer et al.[18] (Sauer: luminosity 5 mm² at 3% resolution, angular acceptance 38° to 48°, van Noort: luminosity 3.9 mm² at 2% resolution, angular acceptance 0° to 85°) allowed for an accurate comparison between the count rate predicted above, and the experimental count rate obtained with their DSCEMS spectrometer. They obtained a signal count rate of 17 s^{-1}. This rate was obtained at 4.2% resolution for a enriched Fe sample, located 25 mm from a 60 mCi source. This corresponds to a rate of .75 counts/s ($17\times24/60\times25^2/75^2$) for the present system if the activity and source sample distance are corrected for. We can also adjust for transmission effects. At 4.3% resolution, the Sauer spectrometer should have a luminosity of ~7 mm² (4.3%/3%x5mm²), and our spectrometer should have a luminosity of ~3.4 mm² (4.3%/2%x3.9mm²/2.5). Their count rate would therefore correspond to a count rate of ~0.36, which is in agreement with our predicted count rate of 0.4±40%.

It is worth mentioning that there could exist some signal loss due to a oxide layers. Belozerski et al.[44] found that a layer of Fe(III) oxide of thickness 30-50 Å accumulated on an enriched Fe sample that was subjected to approximately the same conditions as ours. The oxide layer was found to have a recoil free fraction of nearly zero ($f<.01$), and hence, did not produce an observable resonant signal. Stadnik et al.[23] also reported a surface oxide layer with similar characteristics on an enriched Fe sample. Since the oxide layer does not produce its own signal, the layer reduces the effective thickness from which electrons will be detected. As mentioned above, for 4.3% resolution of 7300 eV electrons, we are looking at electrons that originate from a depth range of ~200 Å from the sample surface. An oxide layer, which is of a homogenous thickness of 40 Å, would therefore eliminate 20% (40/200) of the thickness from which detectable electrons could be emitted.

Chapter 7: Suggested Improvements In the Spectrometer

7.1 Reducing Background

There were four significant sources of background, and it should be possible to nearly eliminate all of these. The background due to electron emissions from the grids has not been a problem for other DSCEMS spectrometers, and so it should be possible to completely eliminate this effect. By holding the grids at the maximum potential available from our supplies (-10 kV) for 8 hours, we were able to anneal irregularities in the grid surface. This procedure reduced grid emissions at 6800 volts from levels which caused ion feedback effects in our detector, to 24±2 counts/s. Subsequent attempts to reduce this background further were ineffective, but an easily implemented possibility for reducing grid emissions further would be to carry the procedure out at higher potentials for longer periods of time.

With sufficient shielding of the source from the detector, background due to non-resonant γ-rays can also be greatly reduced. Two layers of lead are used to separate the source from the detector. The first is inside the collimator tube, and is 4 mm thick, and the second is between the collimator tube, and the top of the chamber, and is 3 mm thick. The combination of 7 mm of lead together with the 8 mm of aluminum from the chamber lid, were unable to sufficiently shield the detector, over 250 mm away. The radiation length in lead is ~10 mm for 136 keV γ-rays (the 136 keV γ-rays are the most penetrating component of the ^{57}Co γ-ray spectrum). The background produced from this source was 8±2 counts/s. It was not possible to insert a thicker layer of lead between the collimator tube and the top of the chamber, and therefore, it will be necessary to increase the width of the collimator tube to ~10 mm. It should be possible to completely eliminate this source of background (8±2 counts/s).

Background due to photoelectrons could be greatly reduced by constructing a new sample chamber which will allow the γ-ray beam to be more shielded from the sample holder and cylinder. A lead shield should surround the beam, outside of the chamber, to a distance which is as close as possible to the sample without interfering with the acceptance angle area. Toriyama[20] obtained a background of only .1 counts/s/miC with a source sample distance of only 10 mm. This corresponds to a background count rate due to photoelectrons which is approximately 400 times lower than our rate. It should be possible to completely eliminate this source of background (18±2 counts/s).

The remaining background was the inherent background associated with the detector. This could be reduced from 9 counts/s to 4 counts/s if the source of the noise bursts (see section 5.1) was determined and then eliminated, so that the detector could be used at the minimum applied operating potential. It is assumed that the noise bursts are caused by a grounding or electrical contact problem, and are not inherent to the detector.

If all of the above changes are implemented it should be possible to reduce the total background to ~4 counts/s from 59±3 counts/s.

7.2 Increasing the Number of Resonant Events

The most important change that can be implemented is to reduce the source-sample distance. This will involve a change in the design of the sample cylinder. It should though be possible to decrease the source-sample distance from 75 mm to 25 mm, and thereby, improve the signal by a factor of 9. Shortening the distance will result in some distortion in the usual Lorentzian shape of the Mossbauer lines[45], since γ-rays striking the sample can not be assumed to be parallel to the velocities imparted to the source by the transducer. A 6 mm diameter source, 25 mm from a 10 mm diameter sample will incur broadening of not more than 8%, and hence, considering the intensity limitations encountered, it would be advantageous to shorten the source-sample distance. A more active sample (50 mCi-100 mCi) would improve the signal by a factor 2-4, and hence, the combined effect, of shortening the source-sample distance and increasing the activity of the source, could result in an increase in the signal by a factor as large as 36. Improving the signal in this manner will increase the background, and therefore, the changes would have to be made in conjunction with improved shielding (see section 7.1).

7.3 Improving Transmission and Detection

The widest resolution of the spectrometer could be increased from 4.3% to about 6%. The most effective method for increasing the resolution would be to increase the transparent portion of the focusing lens in the direction towards the hemispherical top, thereby increasing the acceptance angle. The change will induce a small tail on the hard side of the resolution curve. That is about ⅓ of the additionally detected electrons will originate from electrons with energy above the pass energy window. A factor of nearly 1.3 can be gained by increasing the maximum resolution to 6%.

The detection efficiency could be increased and by fixing the detector voltage with respect to the canister voltage, V1, so that the incoming electrons have an energy that maximizes the detector efficiency. As was mentioned in section 6.2, this could increase the signal count rate by a factor as large as 2.

7.4 Future Additions

It would be desirable to introduce a cold finger to the system so that low temperature Mossbauer spectra could be obtained. An argon ion gun for in situ cleaning of sample surfaces would enable the removal of ice from low temperature surfaces. As was mentioned earlier, Liljequist et al. found that in a vacuum of $.5\text{x}10^{-7}$ torr, a few hundred A of ice had accumulated on a sample at a temperature of -100°C after several hours. The argon gun would also enable the experimenter to clean oxide layers, and thus improve signal rates.

References

1.H.M. van Noort and A.A. van Gorkum, Journal of Physics E: Scientific Instruments 21 (1988) 587-591.

2.T.E. Cranshaw, B.W. Dale, G.O. Longworth, and C.E. Johnson, Mössbauer spectroscopy and its applications, Cambridge University Press, Cambridge,1985, p.10.

3.Frauenfelder H., The Mossbauer Effect: A Review with a Collection of Reprints, W.A. Benjamin, Inc., 1963.

4.D. Liljequist and T. Fkdahl. University of Stockholm Institute of Physics Report 78 - 17.

5.Liljequist D., Scanning Electron Microscopy/1983/III (997-1017)

6.D.Liljequist and M. Ismail, Physical Review B volume 31, number 7, 4131-4136.

7.R.A. Krakowski, R.B. Miller, Nuclear Instruments and Methods 100 (1972) 93-105.

8.J.Bainbridge, Nuclear Instruments and Methods, 128 (1975) 531-535.

9.G.P. Huffman, Nuclear Instruments and Methods, 137 (1976) 267-290.

10.D. Liljequist. University of Stockholm Institute of Physics Report 85 -20.

11.M. Ismail, and D. Liljequist, Hyperfine Interactions 29 (1986) 1509-1512.

12.Z.W. Bonchev, A. Jordanov and A. Minkova, Nuclear Instruments and Methods, 70 (1969) 36.

13.V. Baverstam, C. Bohm, B. Ringstrom, and T. Ekdahl, Nuclear Instruments and Methods, 108 (1973) 439.

14.T. Toriyama, M. Kikawa, M. Fujioka, and K. Hisatake, Japanese Journal of Applied Physics, Supp.2, Part 1 (1974) 733.

15.T.Shigematsu, H.-D. Pfannes, W. Keune, Mossbauer Spectroscopy and It's Chemical Applications, American Chemical Society, 1981, 125-132.

16.U. Baverstam, B. Bodlund-Ringstrom, C. Bohm, T. Ekdahl, D. Liljequist. Nuclear Instruments and Methods 154 (1978) 401-403.

17.J. Parellada, M.R. Polcari, K. Burin, and G.M. Rothberg, Nuclear Instruments and Methods 179 (1981) 113-118.

18.Ch. Sauer, A. Holzwarth, Zs. Kajcsos, and W. Zinn, Nuclear Instruments and Methods In Physics Research, B34 (1988) 377-382.

19.U. Baverstam. B. Bodlund-Ringstrom, C. Bohm, T. Ekdahl, and D. Liljequist, University of Stockholm Institute of Physics Report 77 - 23.

20.T. Toriyama, K. Asano, K. Saneyoshi, K. Hisatake, Nuclear Instruments and Methods In Physics Research B4 (1984) 170-185.

21.M. Domke, B. Kyvelob, and G. Kaindle, Hyperfine Interactions, 10 (1981) 795.

22.T.S. Yang, B. Kolk, T. Kachnowski, J. Trooster, and N. Benczei-Koller, Nuclear Instruments and Methods 197 (1982) 545-556.

23.Z.M. Stadnik, H.R. Borsje, A.E.M. Swolfs, W.H.A. Leenders, J.C. Fuggle, Review of Scientific Instruments 60(4), April 1989.

24.H.M. van Noort, F.J. Ferguson, C.J.G. Verwer, A.A. van Gorkum, J.M.E. van Laarhoven, and C.J.M. Denissen, Nuclear Instruments and Methods in Physics Research B34 (1988) 391-395.

25.D.A. Huchital, and J.D. Rigden, Journal of Applied Physics 43 (1972) 2291-2302.

26.P. Staib, and U. Dinklage, Journal of Physics E: Scientific Instruments, 10 (1977) 914-921.

27.A.A. van Gorkum, J.Vac.Sci.Technol.B 1 (4), Oct.-Dec. 1983.

28.H. Sato, and M. Mitsuhashi, " A New Detection System with a Microchannel Plate for Energy-Selected Conversion Electron Mossbauer Spectroscopy", J.C. Baltzer A.G. Scientific Publishing Company.

29.T. Myint-U, L. Debnath, Partial Differential Equations for Scientists and Engineers, Elsevier Science Publishers, New York, New York, 1987, p.463.

30.William F. Ames, Numerical Methods for Partial Differential Equations, Thomas Nelson and Sons Ltd., Don Mills, ON, 1969.

31.W.H. Press, B.P. Flannery, S.A. Teukolsky, W.T. Vetterling. Numerical Recipes in C, Cambridge University Press, 1982, p.677.

32.Fischer Connectors Ltd., 28245 Avenue Cocker, Valencia California 91355, (805)295-0600.

33.Araldite epoxy produced by Formulated System Corp., CIBA-GEIGY Corp., 4917 Dawn Ave., East Lansing MI 48823, USA, (517)351-5900.

34.Carbon filled epoxy, identification #60LA/B, manufactured by Emerson & Co., 77 Dragon Court, Woburn MA 01888, (617)938-8630.

35. M.G. Chemical products purchased through Electronsonic Ltd., 1100 Gordon Rd., Willowdale ON, Canada, M2H 3B3, (416)494-1555.

36.G.E. Chemicals insulating varnish purchased through Electrosonic Ltd., 1100 Gordon Rd., Willowdale ON, Canada, M2H 3B3, (416)494-3030.

37.Miniature coaxial cable manufactured by New England Electric Wire Co., model #16644Sp 10Fep Type S.

38.L.Holland, W.Steckelmacher, and J.Yarwood, Vacuum Manual, Halstead Press, New York, New York, 1974, p.4.

39.Gallileo Electro-Optics Corp., P.O. Box 550, Galileo Park, Sturbridge, MA 01566 USA, Telephone:(508)347-9191, Fax:(508)347 3849.

40.Radioactive $^{57}CoCl_2$ solution purchased from Du Pont Canada Inc., 6000 Trans Canadienne, Pointe Clair PQ, H9R 1B9, (613)348-3616.

41.310 Stainless Steel sample purchased through Du Pont Canada Inc., 6000 Trans Canadienne, Pointe Clair PQ, H9R1B9, (613)348-3616.

42. E.A. Kurtz, American Laboratory, March 1979, figure 13

43.L.X. Liao, D.H.Ryan, and Z. Altounian, Review of Scientific Instruments, Accepted for Publication 1993, Table 1.

44.G.N. Belozerski, C. Bohm, T. Ekdahl, and D. Liljequist, Scientific Instruments and Methods 192 (1982) 539-543.

45.J.J.Bara and B.F. Bogacz, Mossb.Eff.Ref.Data J. 3,154 (1980).